

Growth kinetics of siderite at 298.15 K and 1 bar

Clancy Zhijian Jiang*, Nicholas J. Tosca

*Earth Sciences Department, University of Oxford, OX1 3AN,
England, United Kingdom.*

*Corresponding author: zhijian.jiang@linacre.ox.ac.uk

Revised manuscript submitted to Geochimica et Cosmochimica Acta

24th December 2019

10 Abstract

11 The widespread occurrence of siderite at the Earth's surface has motivated in-
12 vestigations into the thermodynamic factors controlling its stability for most of the
13 last century. However, despite a new appreciation for multiple Fe(II)-carbonate min-
14 eralisation pathways, the rates of siderite growth have not been accurately predicted
15 as a function of solution chemistry. This has impeded a quantitative understanding
16 of myriad geochemical systems, both modern and ancient. To address this issue, we
17 investigated the growth kinetics of synthetic siderite seeds in anoxic closed-system
18 conditions at 298.15 K and 1 bar. On the basis of monitoring the chemical evolution
19 of the bulk solutions over the course of 46 days, our results demonstrate two distinct
20 relationships between kinetic behaviour and solution saturation (Ω) with respect
21 to siderite. These relationships are best explained by chemical affinity-based rate
22 laws that have been extensively applied to the growth kinetics of calcite (a mineral
23 isostructural with siderite). More specifically, the surface area-normalised siderite
24 growth rates display a linear correlation with supersaturation ($\Omega - 1$) when $\Omega \gtrsim 5$,
25 suggesting a growth rate controlled by the transport of ions to the mineral surface
26 (r_{tr}):

$$r_{tr} = 10^{-12.60 \pm 0.16} (\Omega - 1)^{1.057 \pm 0.112}.$$

27 At low solution saturation, growth rates are consistent with spiral mechanism-
28 dominated surface reactions (r_{sr}), exhibiting a parabolic correlation with ($\Omega - 1$):

$$r_{sr} = 10^{-13.42 \pm 0.14} (\Omega - 1)^{1.868 \pm 0.307}.$$

29 These data show that at comparable solution saturation at 25 °C, siderite growth
30 is nearly 7-orders of magnitude slower than that of calcite. These kinetic behaviours
31 imply that most examples of natural Fe(II) supply fluxes (e.g., dissimilatory iron
32 reduction, hydrothermal activity, or dissolution of other Fe(II)-minerals) would only
33 be balanced by siderite precipitation rates at very high supersaturation, or, if the
34 barrier to Fe(II)-carbonate nucleation is surpassed, balanced by episodic fluctuations
35 in precipitation rate in response to Fe(II) accumulation. In combination with kin-
36 etic barriers influencing nucleation, this slow growth rate provides a straightforward
37 explanation for the common observation that many anoxic water bodies are persist-
38 ently supersaturated with respect to siderite, and implies that the precipitation of
39 siderite may be more dynamic than previously appreciated.

40	Contents	
41	1 Introduction	1
42	2 Methodology	2
43	2.1 Apparatus and reagent preparation	2
44	2.2 Siderite seed synthesis	3
45	2.3 Growth and reprecipitation experiments	3
46	2.4 Analytical procedures	5
47	3 Results	7
48	3.1 Solution chemistry evolution	7
49	3.2 Solid characterisations	8
50	3.2.1 XRD and FT-IR characterisation	8
51	3.2.2 SEM imaging	12
52	3.2.3 BET-surface area	13
53	4 Discussion	17
54	4.1 Chemical affinity-based rate laws	17
55	4.2 Siderite growth kinetics	20
56	4.3 Comparison with previous siderite kinetic studies	24
57	4.4 Comparison with Ca- and Mg-carbonate growth	27
58	5 Conclusion	30
59	Supplementary information	41
60	S.1 Thermodynamic calculations	41
61	S.2 Carbonate speciation calculation	43

62 List of Tables

63	1 Starting solution compositions of growth and reprecipitation experi-	
64	ments	6
65	2 Evolution of solution chemistry of growth experiments	21
66	3 Evolution of solution chemistry of reprecipitation experiments	22
67	4 Thermodynamic properties and constants	42
68	5 A shortlist of reported values of siderite solubility product	43

69 List of Figures

70	1 Experimental apparatus for siderite seed synthesis	4
71	2 $p\text{CO}_2$ -pH space of closed-system syntheses of siderite	6
72	3 Evolution of solution [Fe(II)] (ICP-MS analysis) in the growth and	
73	the reprecipitation experiments	9
74	4 The evolution of solution saturation and the cumulative Fe(II) con-	
75	sumption (mole) of growth experiments	10
76	5 Powder X-ray diffractograms of seed and harvested solids	11
77	6 FT-IR transmittance spectra of seed and harvested solids	12

78	7	SEM images of siderite seed and harvested solids from growth exper-	
79		iments	15
80	8	SEM images of harvested solids from reprecipitation experiments . .	16
81	9	An illustration of microscopic mineral-water processes a schematic of	
82		kinetic behaviour	19
83	10	Kinetic behaviours of siderite growth	23
84	11	Comparison of siderite growth rates with previous studies	27
85	12	Comparison of growth kinetics between siderite and calcite.	29

1 Introduction

Detailed knowledge of Fe(II)-carbonate crystallisation is crucial in understanding and predicting the behaviour of a wide variety of natural and engineered geochemical systems. For example, because it is essentially ubiquitous in ancient sedimentary rocks (in particular of Precambrian age), siderite is thought to have strongly influenced the biogeochemical cycling of Fe and C throughout much of Earth's history (e.g., Bachan and Kump 2015; Beukes and Gutzmer 2008; Heimann et al. 2010; Holland 2007; Holland 1984; Kaufman et al. 1990; Klein 2005; Raiswell et al. 2011; Rasmussen and Muhling 2018; Tosca et al. 2019). Beyond the Earth, siderite is a common component in pre-terrestrial mineral assemblages found in Martian meteorites (Bridges et al. 2019), and appears locally abundant in ancient sedimentary rocks exposed at the Martian surface (Wray et al. 2016). The formation and dissolution of siderite strongly influence corrosion processes (Ogundele and White 1986), as well as nutrient availability and crop production in modern environmental and agricultural systems (Schwab and Lindsay 1983). More recently, Fe-carbonate crystallisation has assumed a central role in efforts to reduce anthropogenic carbon emissions. These include, for example, the application of basaltic rocks rich in Ca, Mg, and Fe(II) at source point (e.g., power plants) to capture CO₂ via carbonate mineralisation (e.g., Callow et al. 2018; Gislason et al. 2010; Oelkers et al. 2008), as well as the injection of CO₂ saturated-fluids into depleted oil and gas reservoirs (e.g., Xu et al. 2004, 2005).

Although the widespread occurrence of siderite has motivated thermodynamic studies for most of the last century (since Smith 1918), the rates and pathways of Fe(II)-carbonate crystallisation remain poorly understood. For example, geochemists have only recently appreciated that Fe(II)-carbonate precipitation commonly involves multiple solid phases and, as a consequence, various precipitation pathways. Recent experimental studies have shown that homogeneous Fe(II)-carbonate precipitation is commonly initiated by the nucleation of amorphous iron carbonate (AFC) at high supersaturation (e.g., Dideriksen et al. 2015; Jiang and Tosca 2019; Montes-Hernandez and Renard 2016; Sel et al. 2012). Once formed, AFC appears to provide a favourable surface promoting the secondary growth of more stable crystalline phases, including chukanovite (which is metastable with respect to siderite) and/or siderite depending on solution chemistry (Dideriksen et al. 2015; Jiang and Tosca 2019; Montes-Hernandez and Renard 2016; Sel et al. 2012).

However, even though recent work has shown that siderite may be produced through multiple pathways, its growth rate has not been accurately predicted as a function of solution saturation. This has impeded a quantitative understanding of myriad geochemical systems, both modern and ancient. While numerous experimental studies have documented the formation of siderite films on corroding steel (i.e., Burkle et al. 2017), few experiments have derived phenomenological rate laws for seeded siderite growth as a function of solution saturation. Of the handful of studies reporting kinetic data, Wajon et al. (1985) reported Fe(II) removal rates through siderite precipitation

on to Ca- and Mg-containing carbonate minerals, and Greenberg and Tomson (1992) reported the results of seeded siderite precipitation experiments as a function of temperature, but both studies reported insufficient data to constrain the effect of solution saturation at a given temperature. Jimenez-Lopez and Romanek (2004) examined seeded Fe(II)-carbonate growth at room temperature on uncharacterised solids which were homogeneously precipitated from solution before constant chemical conditions were established. However, data are reported only across a high but narrow range of supersaturation. One recent study, Ma et al. (2018), measured heterogeneous siderite growth on an electrochemical quartz crystal microbalance coated with Fe or Au from 50 to 80 °C, and fitted their data with a temperature- and surface activation energy-dependent kinetic model. The Ma et al. (2018) model, however, if extrapolated to room temperature, yields precipitation rates that diverge from those reported in Jimenez-Lopez and Romanek (2004) by more than 5 orders of magnitude at the same solution saturation. The scarcity of room temperature kinetic data also leaves the dominant crystal growth mechanisms of siderite, and the ranges in saturation state over which they operate, largely unknown. This, in turn, prevents a detailed understanding of the links between solution chemistry, crystalline morphology, and isotope/trace element incorporation.

To address these issues, we investigated the growth kinetics of siderite at room temperature and pressure across a wide range of saturation state. In what follows, we present the experimental procedure, observations on solution chemistry, characterisations of solids, and development of kinetic expressions correlating siderite growth rate with solution saturation.

2 Methodology

2.1 Apparatus and reagent preparation

Closed-system siderite syntheses were conducted at 298.15 K within a strictly anoxic Coy polymer glovebox filled with 4 % H₂/96 % N₂ gas and maintained at anoxic conditions by two pairs of palladium catalysts and anhydrous CaSO₄ desiccants. The palladium catalysts scrubbed O₂(g) in the glovebox by continuously reacting trace O₂(g) with available H₂(g) to form H₂O(l), which was subsequently removed by CaSO₄ desiccants. The O₂ and H₂ contents in the glovebox were continuously monitored by a Coy gas analyser to ensure an atmosphere of < 1 ppm O₂ throughout the preparation and storage of stock solutions and samples.

All solutions were prepared using de-ionised water (resistivity 18.2 MΩ·cm) that was first deoxygenated by purging with O₂-free N₂ gas for at least 2 h (Butler 1964), then placed on a stir plate for 24 h in the glovebox to allow any residual O₂ to escape and be removed by the catalysts and desiccants. Metal-stock solutions (1 molal) were prepared by dissolving analytical grade metal-chloride powders in the deoxygenated de-ionised water. FeCl₂ stock solution was treated with Fe⁰ powder (≥ 99 %; Sigma-Aldrich) and HCl (pH < 2) for 24 h to remove any Fe(III) in the stock FeCl₂·4H₂O powder (≥ 99 %; Sigma-

174 Aldrich). The Fe^0 was then removed by running the stock solution through
 175 a polymer container with a high-strength Nd magnet inserted in the wall.
 176 NaHCO_3 stock solutions (0.5 molal; powder $\geq 99.7\%$; Sigma-Aldrich) were
 177 freshly prepared for each batch of experiments to ensure the total dissolved
 178 inorganic carbon (DIC) across experiments was not affected by degassing of
 179 the stock solution over time. KCl was added to all growth experiments as
 180 a reference element to ensure the internal consistency of elemental analyses.
 181 NaCl powder was added to the experiment to balance the stoichiometric ionic
 182 strength for each solution composition.

183 2.2 Siderite seed synthesis

184 Siderite seed was generated in a sealed Teflon reactor constructed outside
 185 of the glovebox for the ease of handling and cleaning (Fig. 1). NaHCO_3
 186 solution (250 mL, 0.2 molal with 0.01 molal NaOH, $\text{pH} \approx 10$) and the FeCl_2
 187 solution (250 mL, 0.1 molal, $\text{pH} \approx 3$) were prepared within the glovebox and
 188 sealed with three-way stopcocks prior to being taken out of the glovebox.
 189 The Teflon reactor and all the tubing were purged with O_2 -free N_2 gas for 10
 190 min and 2 min, respectively, before the reagents were connected. A strictly
 191 anoxic interior atmosphere was achieved by constantly purging the head-space
 192 in the system with N_2 gas throughout the 3-h synthesis. As illustrated in
 193 Fig. 1, through a combination of stopcocks and unidirectional check valves,
 194 FeCl_2 solution was first introduced into the Teflon reactor by N_2 gas, and
 195 the synthesis was initiated by titrating NaHCO_3 solution via a Metrohm 848
 196 Titrino plus autotitrator. The NaHCO_3 solution was titrated at $0.025 \text{ mL}\cdot\text{s}^{-1}$,
 197 a rate low enough for the nucleated AFC precursor to start crystallising into
 198 siderite, but not too low where the solution $\text{CO}_3^{2-}/\text{Fe}^{2+}$ ratio would favour
 199 the crystallisation of chukanovite instead of siderite (Jiang and Tosca 2019).
 200 A typical pH profile of seed synthesis increased from pH 3 to near-neutral
 201 within 1 h and plateaued at $\text{pH} \approx 7.5$ due to the pH-dependent nucleation of
 202 AFC. Upon the completion of seed synthesis, solution in the Teflon reactor was
 203 pressed back into the FeCl_2 container by N_2 gas, sealed and transferred into the
 204 glovebox for filtration. A volume of 550 mL of 5 % HNO_3 acid was introduced
 205 into the reactor (in the same manner as FeCl_2 reagent) prior to any exposure
 206 to the atmosphere for effective removal of residual reagents, the reactor was
 207 then flushed with de-ionised water three times. This method allows a reliable
 208 and consistent production of a large quantity of siderite seed; $\approx 1.5 \text{ g}$ every 4
 209 h.

210 2.3 Growth and reprecipitation experiments

211 Two sets of closed-system experiments were conducted using freshly pre-
 212 pared siderite seed (0.5 g each): growth experiments (G-series) and reprecip-
 213 itation experiments (RP-series). Growth experiments were carried out in 1 L
 214 borosilicate glass reaction vessels wrapped in Al-foil to prevent photo-oxidation
 215 within the glovebox. After the establishment of initial solution chemistry

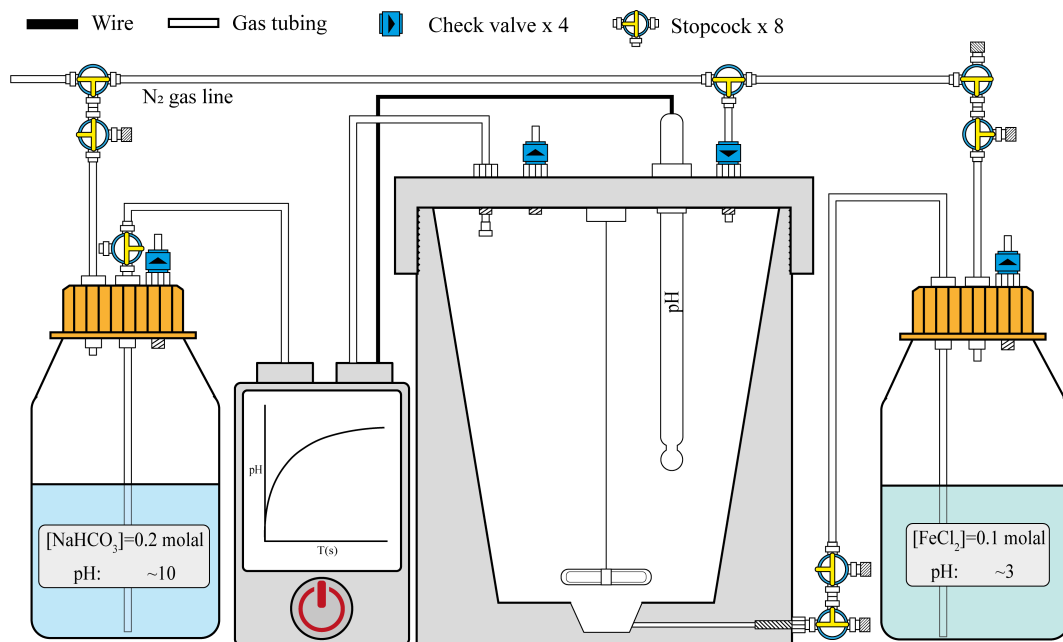


Figure 1: Experimental apparatus for siderite seed synthesis. Reagents were prepared and sealed within an anoxic glovebox. All tubing was purged with N₂ gas for 2 min and the Teflon reactor (600 mL) for 10 min before being connected to reagents. FeCl₂ solution (250 mL) was pressed into the Teflon reactor by N₂ gas, whereas NaHCO₃ solution (250 mL) was titrated at a rate of 0.025 mL·s⁻¹. Upon the termination of synthesis, precipitates and solution were pressed back (by N₂ gas) into the FeCl₂ container and transferred into the glovebox for filtration.

(Table. 1), all solutions were allowed to react over the course of 46 days and gently hand-shaken twice a day. Reprecipitation experiments (RP-series) were designed to replicate growth experiments apart from having no dissolved Fe(II) in the matrices, and allowed to react over the course of 288 days.

The pH of both growth and reprecipitation experiments was held constant by a combination of MOPS (3-(N-morpholino) propanesulfonic acid; 0.05 molal) pH buffer and large DIC pools (up to 0.084 molal). MOPS features significant steric hindrance of acid-base functional groups and therefore exhibits negligible metal complexation (Kandegedara and Rorabacher 1999). MOPS was first added to deoxygenated de-ionised water, and the solution pH was raised to within 0.5 unit of the target value by manual addition of NaOH solution (1 molal), followed by the addition of KCl and NaCl and left for 24 h to homogenise. Predetermined amounts of NaHCO₃ stock solution were then added to the homogenised solution, followed by pH adjustments using a Metrohm 902 Titrando autotitrator (within the glovebox) with NaOH solution (0.5 molal). This procedure was to minimise changes to carbonate speciation associated with pH adjustment. For example, a high proportion of CO₂(aq) in low pH solution would lead to CO₂(g) escape during preparation. To avoid instantaneous nucleation on the entry of the concentrated FeCl₂ solution, the stock solution was first diluted to 0.05 molal before being pipetted into the matrices and gently mixed immediately. In order to minimise CO₂(g) degassing over time, the head-space in the reaction vessels were essentially eliminated (i.e., < 1 mL), and sealed with gas-tight septum caps to facilitate solution sampling. Both the growth and reprecipitation experiments were initiated by the addition of 0.5 g of seed.

Complete starting solution compositions of all experiments are provided in Table. 1. Solution saturations of growth experiments with respect to siderite equilibrium (Singer and Stumm 1970) and the critical supersaturation for homogeneous nucleation of precursor amorphous Fe(II) carbonate (Jiang and Tosca 2019) are illustrated in Fig. 2.

2.4 Analytical procedures

Solution samples (≈ 1.5 mL) were withdrawn through the septum caps of the reaction vessels. To further assure minimum CO₂ degassing into the vacuum caused by solution-extraction, a O₂-free N₂ gas-filled syringe was inserted alongside the sampling syringe to replace the extracted solution volume. The solution samples were then syringe-filtered (0.22 μ m), and an aliquot of 0.5 mL was pipetted into a metal-free polypropylene centrifuge tube with 10 mL of 2 % HNO₃ solution for in-house ICP-MS elemental analysis. All stock solutions were analysed alongside the samples in order to recalibrate the thermodynamic calculations of the actual solution chemistry. The terminal pH measurements indicate < 0.1-unit change over the course of the reaction.

All solids, including the seeds, were filtered out the parent solutions through 0.22 μ m nylon filter membranes and left to dry under the low-humidity anoxic atmosphere in the glovebox for 24 h. Solids harvested from growth experi-

$T = 298.15$ K and 1 bar

Ex.No	pH	MOPS molal $\times 10^3$	KCl molal $\times 10^3$	NaCl molal $\times 10^3$	NaHCO ₃ molal $\times 10^3$	FeCl ₂ molal $\times 10^3$	Ionic strength molal	Initial Ω
G-1	7.515	50.183	2.013	125.617	6.366	0.502	0.176	22
G-2	7.496	50.183	2.009	111.849	20.090	0.502	0.176	66
G-3	7.752	50.009	2.009	120.887	11.071	0.502	0.176	67
G-4	7.378	50.184	2.014	83.491	48.444	0.502	0.176	120
G-5	7.760	50.183	2.024	97.116	35.035	0.502	0.176	217
G-6	7.638	50.184	2.148	48.231	83.739	0.502	0.176	389
RP-1	7.478	50.003	2.000	125.152	6.332	0.000	0.173	—
RP-2	7.496	50.020	2.001	111.499	20.031	0.000	0.174	—
RP-3	7.770	50.009	2.000	120.464	11.036	0.000	0.174	—
RP-4	7.363	50.056	2.002	83.305	48.318	0.000	0.174	—
RP-5	7.742	50.039	2.001	96.658	34.921	0.000	0.174	—
RP-6	7.622	50.100	2.004	48.136	83.604	0.000	0.174	—

Table 1: Starting solution compositions of growth (G) and reprecipitation (RP) experiments. Concentrations of all reagents calculated from added powders and analysed (ICP-MS) stock solutions. Ionic strength calculation includes pH buffer MOPS; $I_{\text{MOPS}} = 0.04$ molal (Buffer Calculator: <http://www.liv.ac.uk/buffers>). Reagents were added to deoxygenated de-ionised water in the order listed in the table (left→right).

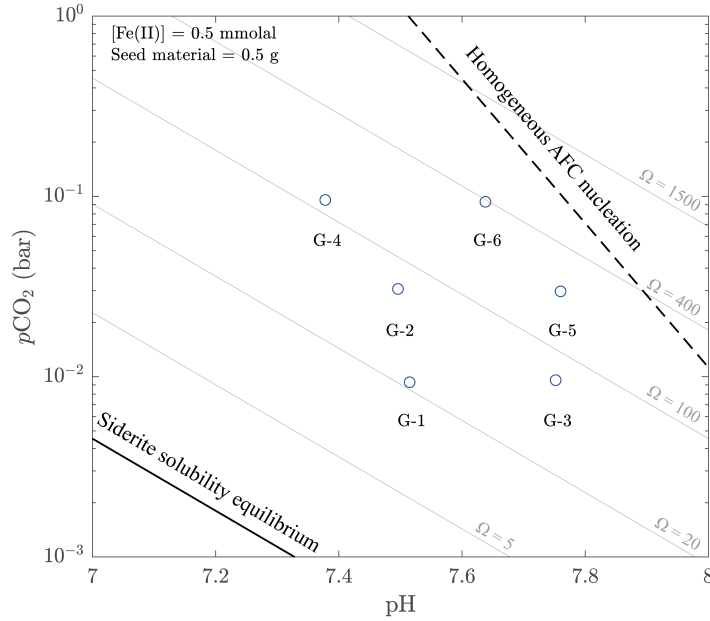


Figure 2: $p\text{CO}_2$ -pH space illustrates the initial solution saturations (Ω) of growth experiments with respect to siderite solubility equilibrium ($\log K_{sp} = -10.24$; Singer and Stumm 1970; solid line) and the critical supersaturation for homogeneous nucleation of amorphous Fe(II) carbonate precursor ($\log IAP_{\text{AFC}} = 2.20$; Jiang and Tosca 2019; dashed line; IAP: ionic activity product). Complete solution compositions are provided in Table. 1. Thermodynamic calculations are provided in Supplementary information.

ments were analysed by powder X-ray diffraction (XRD) using a PANalytical Empyrean Series 2 X-ray diffractometer with a Co $K\alpha$ source, operated at 40 kV and 40 mA, and scanned between 5 and 80 deg 2Θ at a step size of 0.026 deg. Powders were loaded on single-crystal silicon sample holders and sealed with Kapton film within the glovebox to minimise oxidation during XRD analysis. Final X-ray diffractograms are shown with background patterns removed (subtracting patterns obtained on Kapton film).

Fourier transform infrared spectroscopy (FT-IR) analyses were performed on powdered products and were acquired in transmission mode using a PerkinElmer Frontier mid-IR spectrometer. FT-IR transmission measurements were collected on optically transparent KBr pellets with a sample : KBr ratio of $\approx 1 : 200$. KBr powder and sample were ground and compressed into pellets at 7 tons and analysed within 30 min of exposure to air (Fe(III)-O vibrations were closely monitored to ensure minimal oxidation had taken place). Measurements were collected from 400 to 4000 cm^{-1} at 1 cm^{-1} resolution using a deuterated triglycine sulphate (DTGS) detector with a KBr window and beam-splitter.

After identifying oxidation of the solids from growth experiments during sample preparation and analyses (but not during growth experiments), subsequent modifications were made to both XRD and FT-IR procedure for reprecipitation experiments, which is discussed with results in Section. 3.2.1.

In-house scanning electron microscopy (SEM) was performed on all samples to characterise the morphology of the seed and harvested solids. Imaging was conducted using an FEI Quanta 650 FEG SEM in high vacuum mode. To minimise oxidation during sample preparation, small amounts of solid were mounted on adhesive carbon layers on aluminium stubs within the glovebox, then transported to a gold-coating unit in a parafilm-sealed container; sample exposure to air was < 1 minute. Once gold-coated (9 nm Au), samples were immediately transferred into the evacuated SEM-EDS chamber.

The BET-surface area of seed and three harvested solids were measured using a Micromeritics TriStar II Plus surface area and porosity analyser with N_2 gas at a bath temperature of -195.850°C . BET-surface area analysis was conducted at the Surface Analysis Facility, Department of Chemistry, University of Oxford.

3 Results

3.1 Solution chemistry evolution

ICP-MS analyses show monotonic decreases in solution Fe(II) concentrations from all growth experiments (Fig. 3A). A higher initial solution saturation (Ω) corresponds to a higher rate of Fe(II) consumption, and the rate decreases as the solution and solid approach siderite equilibrium (Fig. 4). Importantly, experiments with similar siderite saturations show similar rates of Fe(II) consumption (e.g., G-2 and G-3; Fig. 3A), despite different initial pH- $p\text{CO}_2$ conditions (Fig. 2). Cumulative Fe(II) consumption (in moles) as

303 solution saturation evolved is presented in Fig. 4

304 The solution chemistry of reprecipitation experiments (first 46 days; Fig.
305 3B) shows initial increases in Fe(II) concentrations corresponding to rapid
306 dissolution of nanocrystalline siderite seed (see solid characterisation below),
307 followed by gradual decreases that, though at much lower concentrations, im-
308 itate the saturation-correlated growth kinetics of siderite (Fig. 3A). Although
309 the sampling frequency was too low to constrain the dissolution kinetics of
310 nanocrystalline siderite (completely dissolved in ≤ 3 days), the maximum solu-
311 tion saturation with respect to siderite reached via dissolution was confined
312 to $7 < \Omega < 18$ (Table. 3); at this point in the experiments, the dissolution
313 of nanocrystalline siderite, once complete, was overtaken by the secondary
314 growth of coarsely crystalline siderite.

315 3.2 Solid characterisations

316 3.2.1 XRD and FT-IR characterisation

317 The siderite seed yields a monomineralic X-ray diffractogram and an FT-IR
318 spectrum corresponding to siderite (Fig. 5 & 6). This indicates the initially
319 nucleated AFC rapidly crystallised to siderite during seed synthesis; XRD and
320 FT-IR characterisations of the precursor AFC are provided in Jiang and To-
321 sca (2019). In addition to XRD and FT-IR patterns corresponding to siderite,
322 solids harvested from growth experiments show weak diffraction and absorp-
323 tion peaks that correspond to minor amounts of goethite ($\text{FeO}(\text{OH})$); its peak
324 intensities appear to increase in the order that the samples were analysed (G-1
325 to G-6).

326 As described in the analytical procedure (Section. 2.4), harvested solids
327 from growth experiments were sealed with Kapton film within the glovebox to
328 minimise oxidation. However, due to the scattering of X-rays by Kapton film,
329 the scanning time of each sample was extended to 50 mins to obtain a clear
330 spectrum. This procedure resulted in up to 4 hours and 10 mins exposure to
331 the atmosphere when G-6 was analysed. Pervasive oxidation of solids under
332 Kapton film is observed by the colour change from grey-green to orange-red
333 of the solids at the end of XRD analysis. Kapton film's inability to prevent
334 oxidation has also been reported in the characterisation of synthetic amorphous
335 Fe(II) carbonate by Dideriksen et al. (2015). Similarly, after mixing with
336 KBr powder in the glovebox, grinding and preparing KBr pellet, and FT-IR
337 analysis accounted for ≈ 30 mins exposure to the atmosphere for each sample,
338 cumulatively 2 hours and 30 mins when G-6 was analysed.

339 To test the hypothesis that siderite oxidation occurred during sample ana-
340 lysis and not in the glovebox during crystal growth experiments, solids from
341 reprecipitation experiments (RP series) were treated with extra precaution.
342 For both XRD and FT-IR analyses, only one sample was taken out of the
343 glovebox each time. Individual XRD analysis was conducted without Kapton
344 film, which allowed a significantly reduced scanning time (19 mins). KBr-
345 sample mixture was ground within the glovebox before individually taken out
346 for pellet preparation and analysis. All reprecipitation experiments show X-

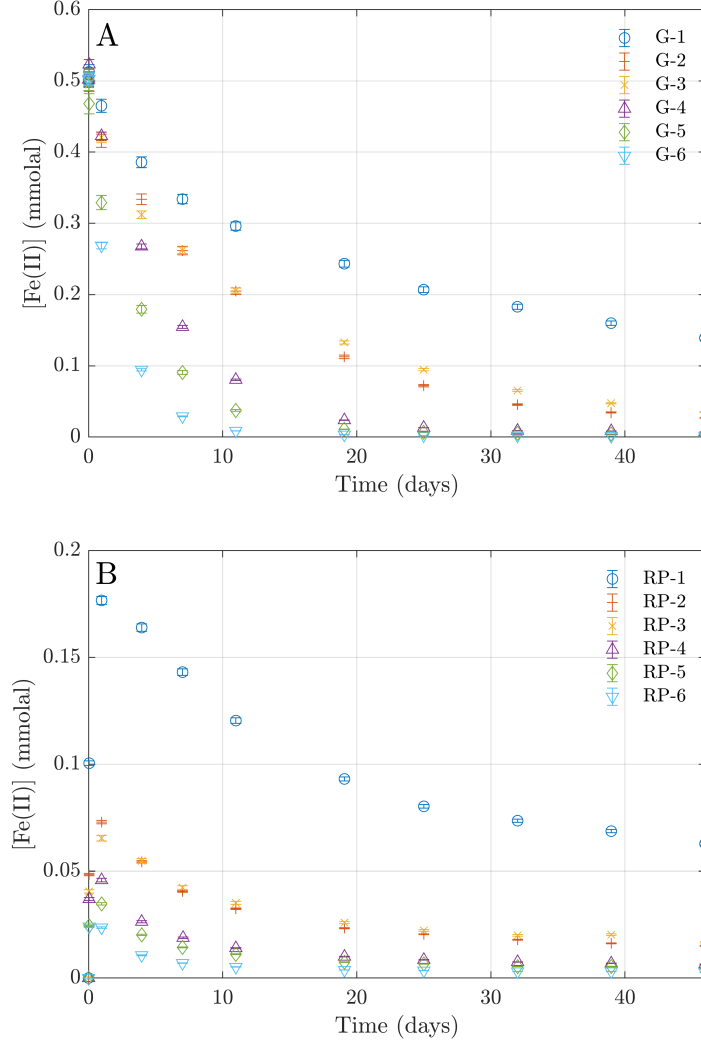


Figure 3: Evolution of solution $[\text{Fe(II)}]$ (ICP-MS analysis) in (A) the growth experiments (G series) and (B) the reprecipitation experiments (RP series; first 46 days). The reprecipitation experiments are exact replica of the growth experiments except that their initial $[\text{Fe(II)}] = 0$ mmolal. Analytical errors (3σ) are $< 3\%$ of measurements.

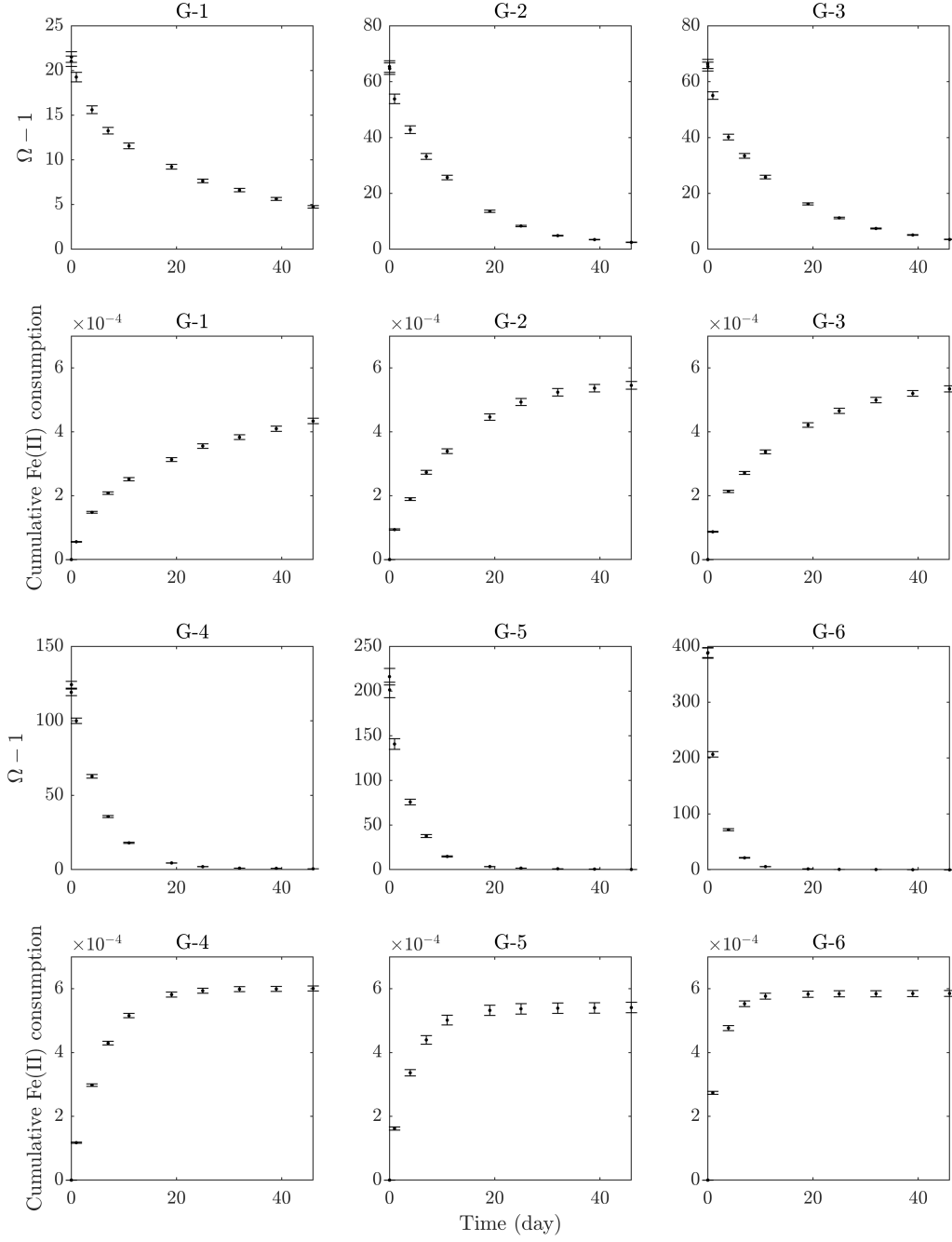


Figure 4: The evolution of solution saturation (Ω) and the cumulative Fe(II) consumption (in moles) of growth experiments. Error bars are 3σ , σ_{Ω} is calculated by assuming $\sigma_{[\text{CO}_3^{2-}]} = \sigma_{[\text{Fe}^{2+}]}$; calculations shown in Supplementary information.

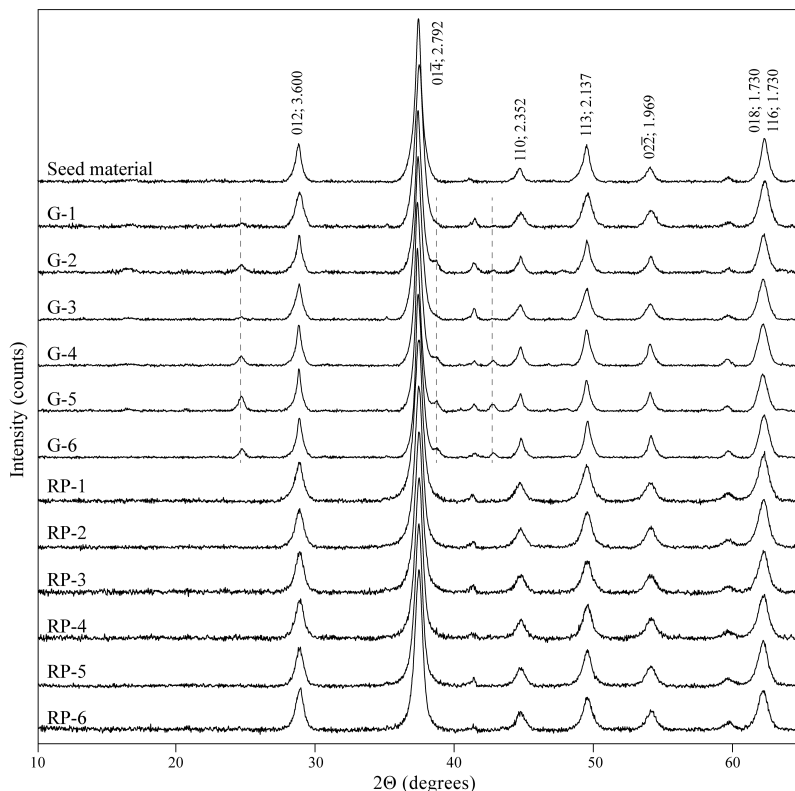


Figure 5: Powder X-ray diffractograms (Co $K\alpha$ source) of siderite seed and the growth experiments (G-series) harvested after 46 days (Kapton film background removed; 50 min scanning time) and reprecipitation experiments (RP-series) harvested after 288 days (no Kapton film, 19 mins scanning time). All solids show diffraction peaks corresponding to siderite, labelled with Miller indices and d -spacing (\AA). Dashed lines indicate the minor occurrence of goethite ($\text{FeO}(\text{OH})$) in the harvested solids from growth experiments but absent in reprecipitation experiments. The origin of goethite is discussed in Section. 3.2.1.

ray diffractograms and FT-IR spectra corresponding to pure siderite (Fig. 5 & 6).

The absence of goethite in the reprecipitation experiments rules out the possibility of goethite formation by (1) residual $\text{O}_2(aq)$ in the matrix solution, and (2) trace $\text{O}_2(g)$ in the glovebox atmosphere that diffused through the septum cap over the course of experiments, because (1) growth and reprecipitation were prepared with same deoxygenated matrix solutions and reagents and (2) reprecipitation experiments resided in the glovebox over a period of 288 days, compared to 46 days of growth experiments. Importantly, the cumulative $\text{Fe}(\text{II})$ consumption in all growth experiments was governed by solution saturation with respect to siderite (Fig. 4). Therefore, we reason that the kinetic constraints obtained from the evolution of solution chemistry can be solely attributed to the precipitation of siderite, and the formation of goethite likely occurred during solid sample drying, preparation, and analyses.

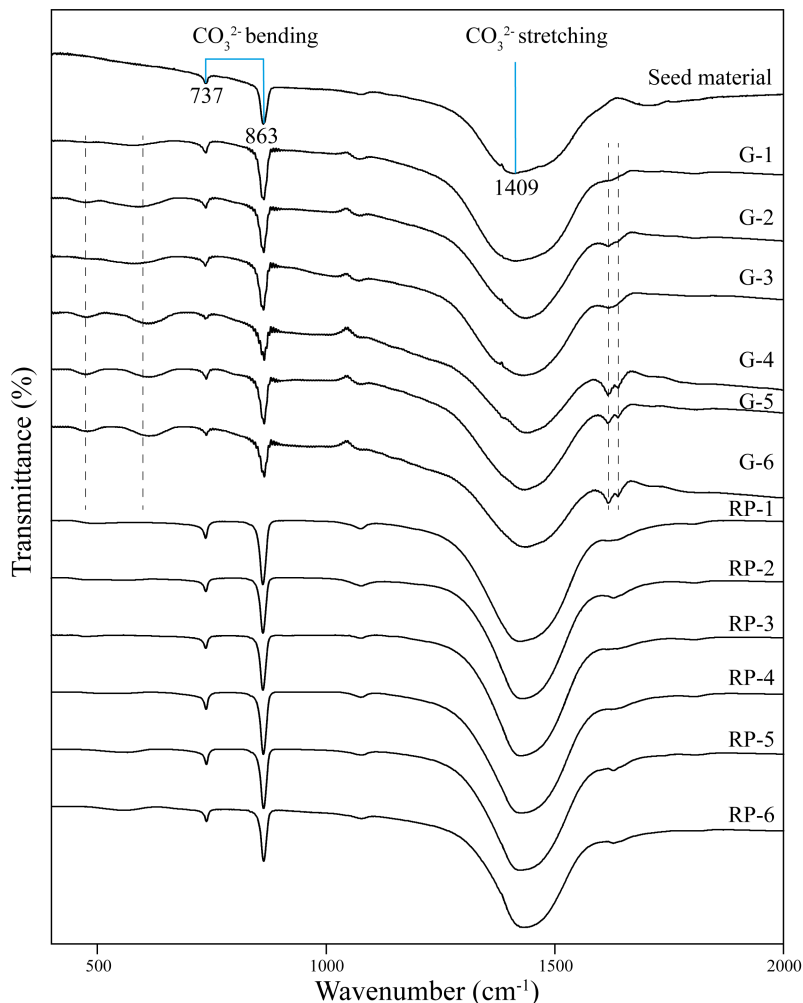


Figure 6: FT-IR transmittance spectra of seed and harvested solids. Solids from growth experiments (G) show the absorption peaks corresponding minor occurrences of goethite (dashed lines) that is absent in the reprecipitation experiments (RP). The origin of goethite is discussed in Section. 3.2.1

3.2.2 SEM imaging

The unreacted siderite seed is dominated by spherical particles of $\approx 2\ \mu\text{m}$ in diameter, with a minor occurrence ($< 5\%$) of $\approx 10\text{--}15\ \mu\text{m}$ larger population (Fig. 7A&B). Neither of the two populations displays discernible crystal morphology, suggesting the seed particles are aggregates of nanocrystalline siderite nuclei. The surface of some $\approx 10\ \mu\text{m}$ spheres shows partially formed globules ($\approx 2\ \mu\text{m}$; Fig. 7A), indicating an early stage of rhomb formation.

After 46 days, solids from growth experiments show two types of crystalline siderite. (1) Interlocking siderite rhombs that are $\leq 50\ \text{nm}$ in edge length; these are observed on all harvested solids (e.g., Fig. 7F&H). The formation of the interlocking small siderite rhombs can be attributed to the crystallisation of seed particles themselves. (2) Overgrown siderite rhombs of edge length $\leq 200\ \text{nm}$ on the surface of seed particles. This population is interpreted to

result from localised growth from the oversaturated solutions. The degree of siderite overgrowth is qualitatively consistent with the initial solution saturation. At the lowest initial saturation, G-1 is dominated by interlocking small siderite rhombs (Fig. 7C&D). With increasing initial saturations, G-2 (Fig. 7E&F), G-3 (Fig. 7G&H), G-4 (Fig. 7I&J), and G-5 (Fig. 7K&L) show the overgrown siderite crystals increase both in size and abundance, as well as a better-developed rhombohedral morphology. Finally, G-6 (Fig. 7M&N) shows complete encrustation of overgrown siderite rhombs of ≈ 200 nm in edge length.

Similar observations can be made from the reprecipitation experiments (288 days), that the seed particles crystallised into interlocking small siderite rhombs (≤ 10 nm) with various degrees of siderite overgrowth (≤ 200 nm) from oversaturated solutions (Fig. 8). However, as indicated by solution chemistry (Fig. 3B), reprecipitation experiments first underwent dissolution of nanocrystalline siderite seeds and followed by secondary growth. Therefore, the degree of siderite overgrowth on the seed particles was not only tied to the supersaturation but also the amount of Fe(II) released via dissolution. For example, because of the high solution pH and DIC, RP-6 reached the highest solution saturation ($\Omega = 18$) with the least amount of seed dissolution ($d[\text{Fe(II)}] = 0.0241 \times 10^{-3}$ molal; Table. 3); SEM imaging of RP-6 show interlocking small siderite but an insignificant amount of overgrowth (Fig. 8F).

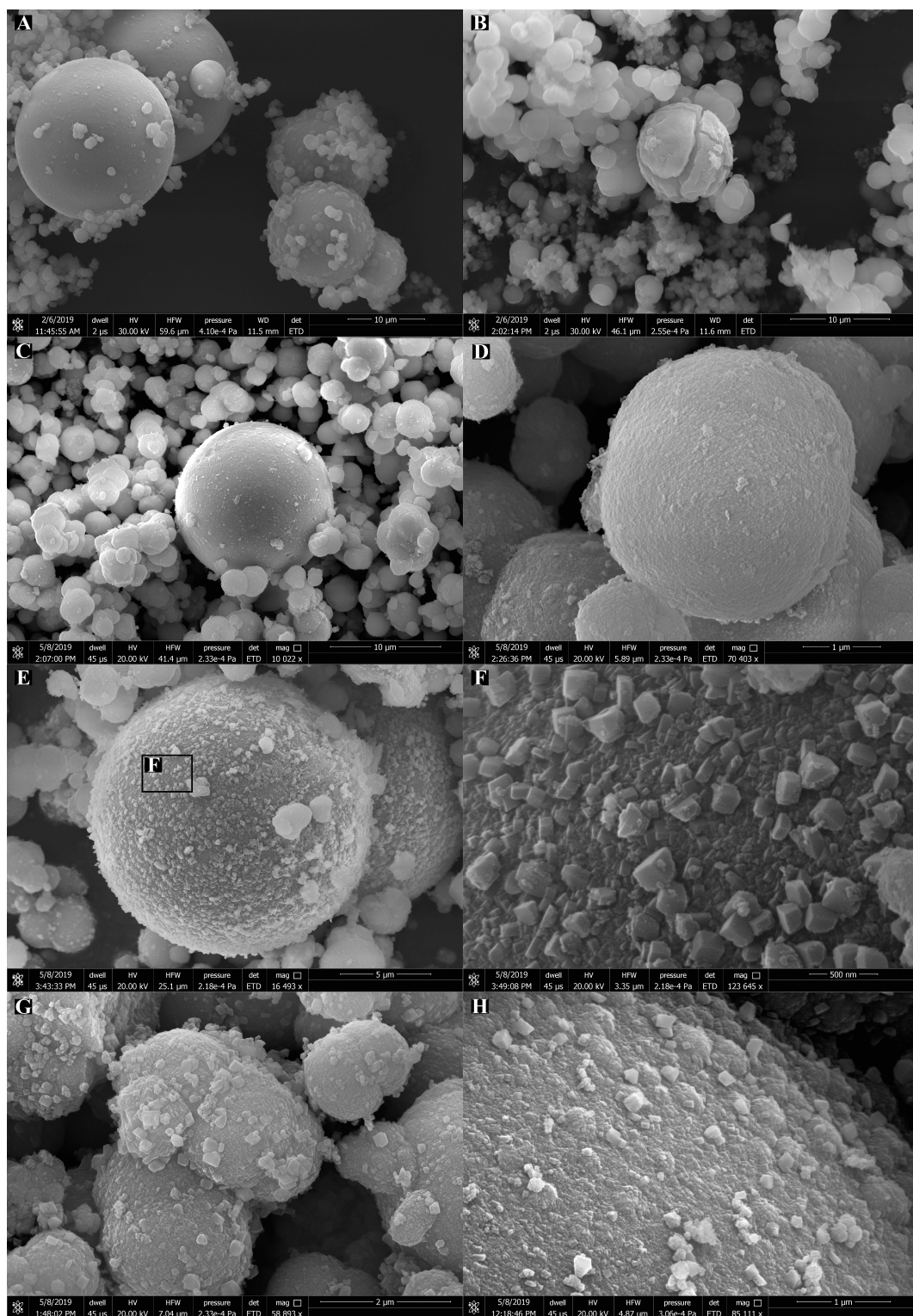
It is important to note that the diameters of both size-populations (≈ 2 μm and ≈ 10 – 15 μm) of seed particles were retained after growth and reprecipitation experiments, and the acicular needle morphology that is typical of water-column goethite precipitation was not observed in all harvested solids (a total of 50 SEM images).

3.2.3 BET-surface area

Surface analyses show the unreacted siderite seed has a BET surface area (A_{BET}) of $109.75 \text{ m}^2 \cdot \text{g}^{-1}$ and a micropore volume (v_{pore} ; t-Plot) of $1.788 \text{ mm}^3 \cdot \text{g}^{-1}$. Three solids harvested from growth experiments show reductions in both surface area and micropore volume; G-2: $A_{\text{BET}} = 82.48 \text{ m}^2 \cdot \text{g}^{-1}$, $v_{\text{pore}} = 0.036 \text{ mm}^3 \cdot \text{g}^{-1}$, G-4: $A_{\text{BET}} = 81.12 \text{ m}^2 \cdot \text{g}^{-1}$, $v_{\text{pore}} = 0.074 \text{ mm}^3 \cdot \text{g}^{-1}$, and G-6: $A_{\text{BET}} = 81.39 \text{ m}^2 \cdot \text{g}^{-1}$, $v_{\text{pore}} = 0.076 \text{ mm}^3 \cdot \text{g}^{-1}$. Though lacking measurements on the evolution of the surface area during growth experiments, the changes in the surface area can be correlated with the amounts of siderite growth, which themselves were stoichiometrically equivalent to the changes in solution Fe(II) concentrations: $\Delta A_{\text{BET}} \propto \Delta[\text{Fe(II)}]$. By fitting the BET-surface area of siderite seed and the end values of three harvested solids, scaling to the ratio of the mass of precipitated siderite (m_{ppt}) over the mass of siderite seed (m_{seed}), the following relation can be established:

$$A_{\text{BET}} = -211.39 \left(\frac{m_{\text{ppt}}}{m_{\text{seed}}} \right) + 109.41, \quad (1)$$

with $R^2 = 0.97$ ($n = 3$). Eq. 1 is used to estimate the BET-surface area of all the solids at each sampling time, against which the growth rates are



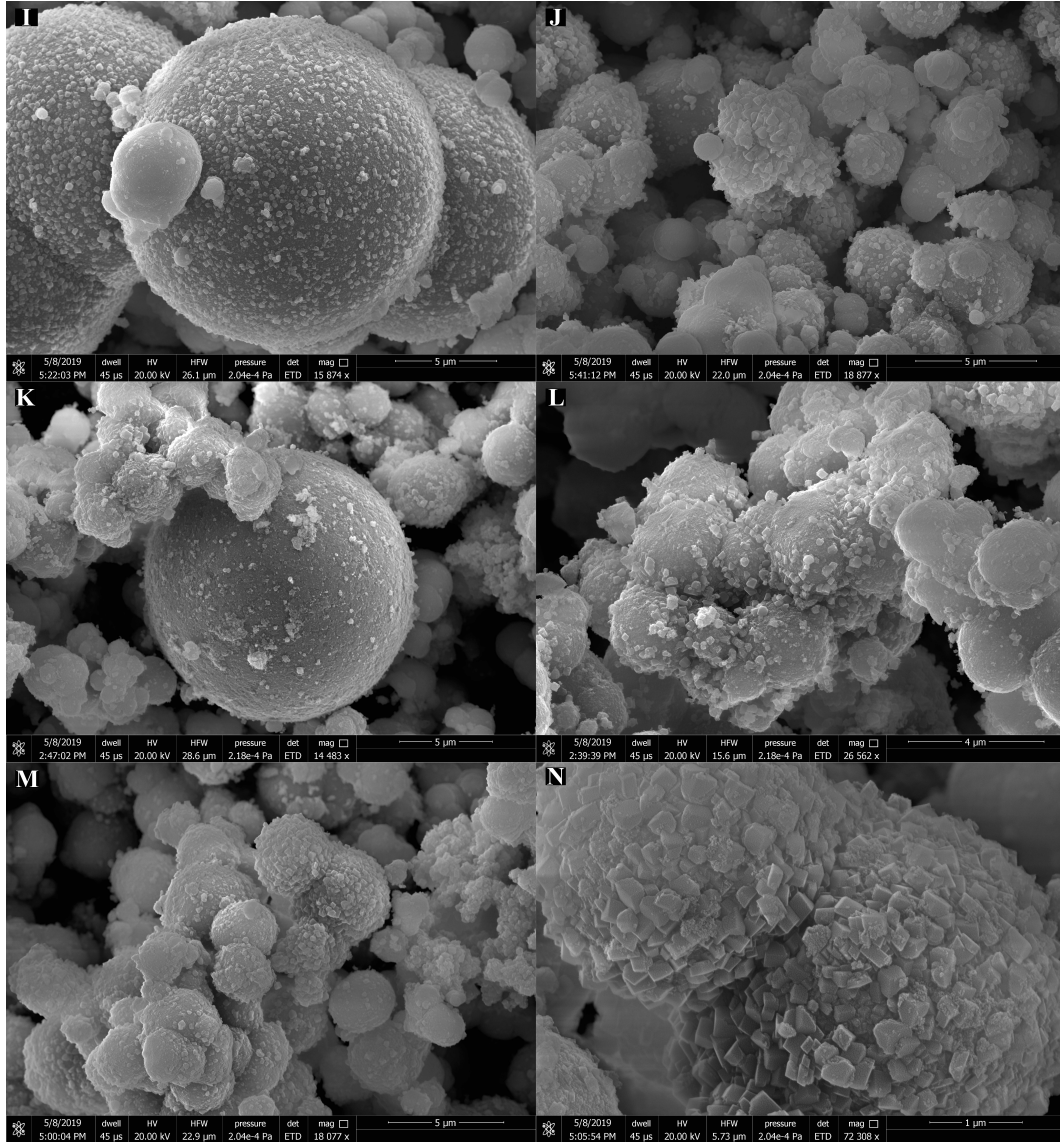


Figure 7: SEM images of siderite seed and harvested solids from growth experiments (46 days). (A&B) Siderite seeds, predominantly composed of spherical particles of $\approx 2 \mu\text{m}$ in diameter with a minor occurrence ($\leq 5 \%$) of larger particles of $\approx 10\text{--}15 \mu\text{m}$ in diameter. (C&D) G-1 shows minor siderite encrustation ($\leq 20 \text{ nm}$ in edge length). With increasing initial solution saturation, G-2 (E&F), G-3 (G&H), G-4 (I&J), and G-5 (K&L) show siderite encrustation increases both in size and abundance, as well as a better-developed rhombohedral morphology. (M&N) G-6 shows complete encrustation of siderite rhombs of $\approx 200 \text{ nm}$ in edge length.

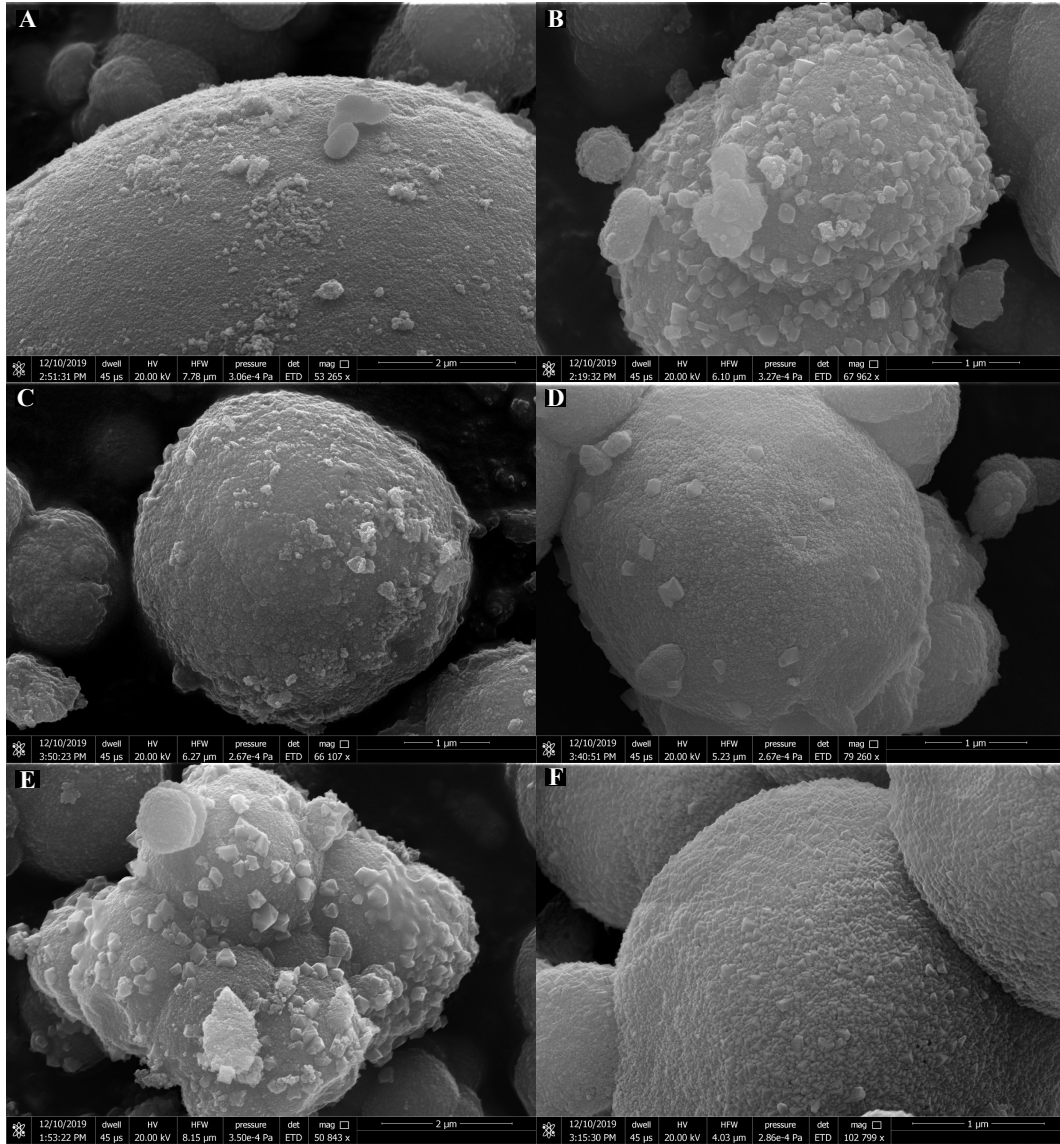


Figure 8: SEM images of harvested solids from reprecipitation experiments (288 days). RP-1 (A) and RP-6 (F) show crystallised seed particles of interlocking small siderite rhombs that are ≤ 10 nm in edge length. RP-2 (B), RP-3 (C), RP-4 (D), and RP-5 (E) show various degrees of localised growth of rhombohedral siderite crystals of edge length ≤ 200 nm, in addition to the crystallised surface of the seed particles.

416 normalised (Table. 2).

417 The same approximation, however, cannot be applied to the reprecipitation
418 experiments as they underwent both dissolution and growth. These processes
419 complicate the evolution of the surface area and its correlation with solution
420 chemistry. Therefore, the secondary growth rates from reprecipitation experi-
421 ments are only normalised against the initial surface area of the siderite seed
422 $A_{BET} = 109.75 \text{ m}^2 \cdot \text{g}^{-1}$ (Table. 3).

423 4 Discussion

424 4.1 Chemical affinity-based rate laws

425 Since the publication of the influential Burton, Cabrera, and Frank crystal
426 growth theory (Burton et al. 1951), numerous mechanistic models have been
427 further developed to correlate the kinetic behaviour of mineral-water inter-
428 actions with solution chemistry. The most widely applied are the chemical
429 affinity-based rate laws (e.g., Aagaard and Helgeson 1982; House 1981; Lasaga
430 1984; Nancollas and Reddy 1971; Nielsen 1984), which generalise growth and
431 dissolution kinetics as a function of energetics (free energy of reaction ΔG_r ,
432 or as $\Omega = \exp \frac{\Delta G_r}{RT}$), and can be cast in the following general formalism (e.g.,
433 Nielsen 1984):

$$\text{rate} = k(\Omega - 1)^n / (1 - \Omega)^n, \quad (2)$$

434 where k is the rate constant, and n indicates the reaction order of growth rate
435 on supersaturation ($\Omega - 1$), or dissolution rate on undersaturation ($1 - \Omega$).
436 The following discussion focuses on crystal growth.

437 Experimentally derived reaction orders (n) from macroscopic precipitation
438 (i.e., solution chemistry) have been ascribed to the following rate-determining
439 microscopic processes associated with the transfer of the constituent ions (sum-
440 marised from Lasaga 1998; Nielsen 1981; Nielsen and Toft 1984; van Cappellen
441 1991):

- 442 1. From the bulk solution to the mineral-water interface.
- 443 2. From the solution into an adsorption layer.
- 444 3. From the solution or an adsorption layer to surface defects and sub-
445 sequent integration into the crystal lattice.
- 446 4. From the solution or an adsorption layer to or to form surface nuclei.

447 These processes are though to contribute to overall reaction rates in the
448 following ways:

- 449 1. Transport-controlled growth rates are linearly dependent on diffusion:
450 $\text{rate} \propto (\Omega - 1)$ (Mullin 1972; Nielsen 1964)

2. Surface-controlled growth by adsorption, with rates linearly dependent on diffusion: rate $\propto (\Omega - 1)$ (Nancollas and Reddy 1971; Nielsen 1983, 1984; Nielsen and Christoffersen 1982; Shiraki and Brantley 1995)
3. Surface-controlled growth at crystal defects dominated by spiral growth, which follows a parabolic rate law: rate $\propto (\Omega - 1)^2$ (Nancollas 1979; Nielsen 1981; Shiraki and Brantley 1995)
4. Surface nucleation that follows an exponential dependence on saturation: rate $\propto \exp(-\frac{U}{\ln \Omega})$, where U incorporates the molar properties and the geometry of nuclei (Christoffersen and Christoffersen 1992; Hillig 1966; Nielsen 1984; Shiraki and Brantley 1995; van Cappellen 1991).

Process (1) is a transport process, and (2–4) can be grouped as surface reaction mechanisms. Typically, the kinetic behaviour of crystal growth is simultaneously influenced by two or more of these processes. An important distinction is that those surface reactions are parallel mechanisms—their individual rates are added, and the faster is the rate-determining mechanism. In contrast, transport and surface reactions are consecutive processes—the slower one is the rate-determining process (e.g., Nielsen 1984).

At low supersaturation, surface reactions proceed at defect sites including step edges, kink, ledge, and hillock/adatom, where the adsorbed ions are preferentially integrated into crystal lattice (e.g., Burton et al. 1951; Lasaga 1998; Nielsen 1984; van Cappellen 1991; Watkins et al. 2017). Because step and kink sites are the most abundant defect sites on crystal surface (Burton et al. 1951; Zhang and Nancollas 1990, 1998), growth at defects is commonly observed to be dominated by a spiral growth spiral mechanism ($n \cong 2$) (Nancollas 1979; Nielsen 1981; Saldi et al. 2009; Shiraki and Brantley 1995; Teng et al. 2000; van Enkevort et al. 1981). In the absence of favourable surface structure, or if the energetics of the system do not favour growth at defects, growth by adsorption ($n = 1$) may become the dominant mechanism (Nielsen 1983, 1984). Growth by adsorption has been used to successfully model quartz dissolution and precipitation across a wide range of solution saturation and temperature (Rimstidt and Barnes 1980), but has only been documented for calcite precipitation near-equilibrium (Nancollas and Reddy 1971; Shiraki and Brantley 1995). As supersaturation increases, surface nucleation will, from a certain point on, become the more efficient growth mechanism (e.g., calcite growth; Shiraki and Brantley 1995; Teng et al. 2000).

Because surface reaction rates (apart from adsorption) are high-power functions of supersaturation, deviation from equilibrium increases reaction rates drastically; this consumes ions in the surface fluid faster than they can be homogenised with the bulk solution. This process establishes a diffusive zone where the surface fluid is maintained at equilibrium by fast surface reactions, and the saturation state in the diffusive zone increase towards the bulk solution (Fig. 9). In this scenario, the rate of surface reactions is capped by the transport of the ions through the diffusive zone, and the overall kinetic behaviour of the system becomes transport-controlled (e.g., DePaolo 2011; Mullin

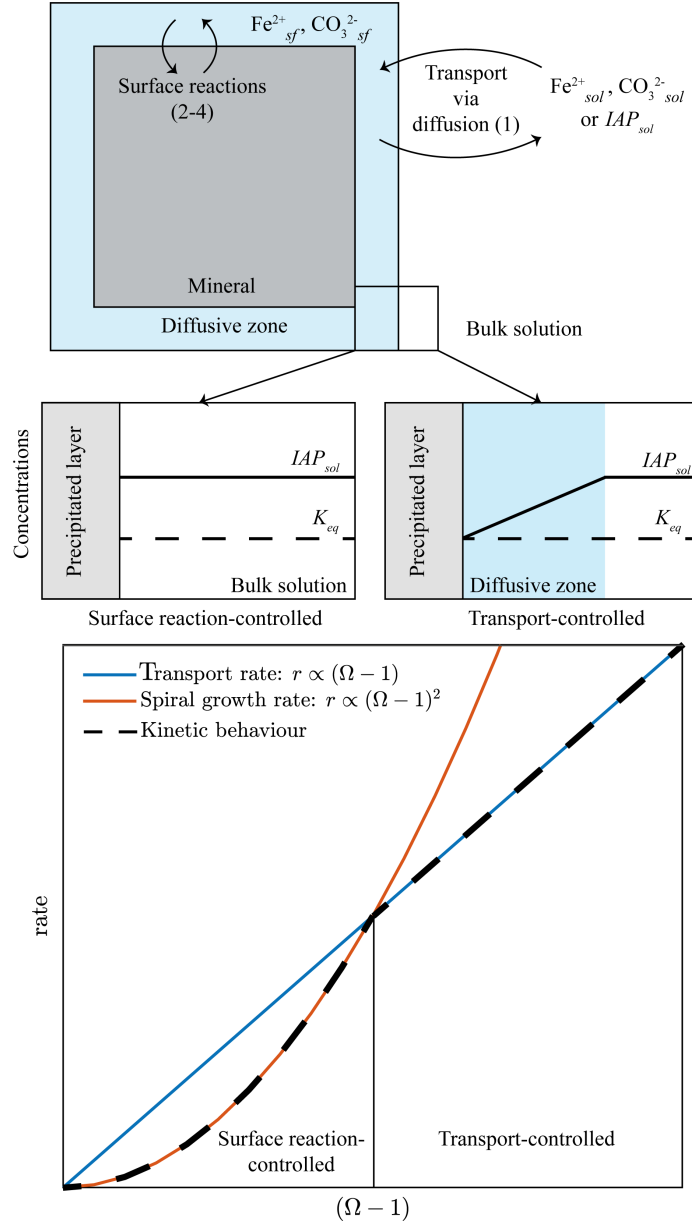


Figure 9: An illustration of microscopic processes at the mineral-water interface (above) and a schematic of the overall kinetic behaviour of the system (below). Water-mineral interactions (exemplified here is crystal growth) follows the surface reaction kinetic model summarised by DePaolo (2011). At low supersaturation, the kinetic behaviour is determined by surface reactions rate, while the solution is sufficiently homogenised (left column). At high supersaturation, a fast surface reaction rate drives the surface fluid (*sf*; in blue) in proximity to the mineral surface to equilibrium, creates a diffusive zone where the transport of dissolved species from the bulk solution (*sol*) becoming the slowest process (right column). The overall kinetic behaviour (dashed line) is dictated by the slowest process, thus, can be cast as surface reaction-controlled versus transport-controlled as a function of supersaturation.

1972; Nielsen 1984; Shiraki and Brantley 1995; van Cappellen 1991; Watkins et al. 2017). This phenomenon can be illustrated by plotting rate $\propto (\Omega - 1)$ and rate $\propto (\Omega - 1)^2$ in Fig. 9, indicating that transport-controlled kinetic behaviour is expected in conditions far from equilibrium.

4.2 Siderite growth kinetics

The growth rate (r ; mole \cdot m $^{-2}$ \cdot s $^{-1}$) of siderite is calculated here as the difference in [Fe(II)] divided by the time lapse between sampling and normalised against the BET-surface area. To calculate the evolving solution saturation during siderite precipitation, a stoichiometrically equivalent amount (to $\Delta[\text{Fe(II)}]$) of carbon is subtracted from the total DIC, followed by calculation of the remaining $[\text{CO}_3^{2-}]$ and supersaturation (Supplementary information, S.2); assuming relatively rapid re-equilibration of carbonate species and no $\text{CO}_2(g)$ exchange. These calculations permit us to assign an average growth rate over the sampling interval to the solution saturation at the time of sampling. All measured and calculated values for growth and reprecipitation experiments are listed in Tables 2 and 3, respectively.

Taking the logarithmic form of the general chemical affinity-based rate law (Eq. 2):

$$\log \text{rate} = \log k + n \log (\Omega - 1),$$

kinetic data from growth experiments (53 data; Table. 2) can be fitted to obtain n as the gradient, and k as the intercept:

$$r = 10^{-12.92 \pm 0.10} (\Omega - 1)^{1.223 \pm 0.10}, \quad (3)$$

with 95 % confidence bound, $R^2 = 0.94$, and the sum of squared errors of prediction (SSE) of 2.386. The fitted equation indicates an overall mixed transport- and surface reaction-controlled kinetic behaviour, with the former being the dominant.

It is, however, noticeable that the growth rate deviates from the Eq. 3 at low supersaturation (e.g., $\Omega \lesssim 5$; Fig. 10A). Such deviation may reflect a transition from transport-controlled growth to surface reaction-controlled as the system approaches equilibrium. However, due to the sparsity of low-supersaturation kinetic data from the growth experiments, a rate law in this growth region can not be established with confidence (i.e., 16 data at $\Omega 5$ yield a $R^2 = 0.76$).

Given the theoretical derivation summarised above and the observations that the reprecipitation experiments were capped to a confined range of low supersaturation ($7 < \Omega < 18$; Table. 3), we reason that the secondary growth in reprecipitation experiments was controlled by surface reactions (r_{sr} ; $n \approx 2$) instead of transport. This interpretation is supported by the fitted equation (Fig. 10B; 48 data):

$$r_{sr} = 10^{-13.42 \pm 0.14} (\Omega - 1)^{1.868 \pm 0.307}, \quad (4)$$

with 95 % confidence bounds, $R^2 = 0.78$, and $SSE = 3.994$. This kinetic-saturation correlation ($n = 1.868$) indicates that siderite growth at low supersaturation is likely dominated by spiral mechanism. A further differentiation

$I = 0.175$ molal; $T = 298.15$ K and 1 bar

Ex.No	Time h	[Fe(II)] molal $\times 10^3$	[DIC] molal $\times 10^3$	$[\text{CO}_3^{2-}]$ molal $\times 10^6$	BET surface area $\text{m}^2 \cdot \text{g}^{-1}$	Ω	Growth rate $\text{mol} \cdot \text{m}^{-2} \cdot \text{s}^{-1}$ $\times 10^{12}$
G-1 pH=7.515	0.77	0.5127	6.366	23.595	109.75	22.5	—
	22.95	0.4650	6.318	23.419	109.41	20.3	12.984
	94.70	0.3858	6.239	23.125	107.24	16.6	6.952
	167.98	0.3340	6.188	22.933	102.69	14.3	4.577
	263.38	0.2962	6.150	22.793	99.71	12.6	2.621
	457.72	0.2433	6.097	22.597	97.53	10.2	1.854
	599.68	0.2069	6.060	22.462	94.51	8.6	1.789
	767.48	0.1829	6.036	22.373	92.42	7.6	1.009
	935.25	0.1599	6.013	22.288	91.05	6.6	0.980
	1103.07	0.1390	5.992	22.210	89.73	5.7	0.902
G-2 pH=7.496	0.83	0.4964	20.084	71.107	109.75	65.6	—
	23.02	0.4160	20.004	70.822	109.06	54.8	22.489
	94.73	0.3338	19.922	70.531	104.43	43.9	7.429
	168.05	0.2617	19.850	70.276	99.72	34.2	6.648
	263.42	0.2049	19.793	70.075	95.58	26.7	4.169
	457.75	0.1126	19.701	69.748	92.33	14.6	3.515
	599.72	0.0721	19.660	69.605	87.07	9.3	2.166
	767.55	0.0454	19.633	69.510	84.76	5.9	1.225
	935.32	0.0345	19.623	69.472	83.25	4.5	0.507
	1103.13	0.0269	19.615	69.445	82.63	3.5	0.351
G-3 pH=7.752	0.73	0.4951	11.064	72.088	109.75	66.4	—
	22.92	0.4206	10.990	71.602	109.00	56.0	20.776
	94.68	0.3120	10.881	70.895	104.70	41.1	9.938
	167.95	0.2622	10.831	70.570	98.48	34.4	4.596
	263.37	0.2054	10.774	70.200	95.62	26.8	4.161
	457.70	0.1328	10.702	69.727	92.36	17.2	2.729
	599.67	0.0946	10.664	69.478	88.22	12.2	2.010
	767.45	0.0654	10.634	69.288	86.05	8.4	1.324
	935.22	0.0474	10.616	69.171	84.39	6.1	0.827
	1103.03	0.0350	10.604	69.090	83.36	4.5	0.574
G-4 pH=7.378	0.90	0.5231	48.444	128.728	109.75	125.3	—
	23.08	0.4226	48.343	128.461	109.41	100.9	28.032
	94.77	0.2676	48.188	128.049	104.81	63.7	14.591
	168.12	0.1547	48.075	127.749	95.93	36.7	11.127
	263.45	0.0804	48.001	127.551	89.47	19.1	5.903
	457.78	0.0237	47.944	127.401	85.23	5.6	2.296
	599.75	0.0131	47.934	127.373	82.00	3.1	0.587
	767.62	0.0089	47.930	127.361	81.40	2.1	0.201
	935.38	0.0084	47.929	127.360	81.16	2.0	0.022
	1103.20	0.0071	47.928	127.357	81.13	1.7	0.061
G-5 pH=7.760	0.80	0.4679	35.001	232.382	109.75	202.3	—
	22.98	0.3291	34.862	231.461	107.44	141.6	40.771
	94.72	0.1792	34.712	230.466	99.47	76.9	14.876
	168.02	0.0906	34.624	229.877	90.89	38.7	9.103
	263.40	0.0374	34.570	229.524	85.83	16.0	4.354
	457.73	0.0109	34.544	229.348	82.79	4.6	1.081
	599.70	0.0067	34.540	229.320	81.28	2.9	0.232
	767.52	0.0051	34.538	229.309	81.05	2.2	0.079
	935.28	0.0042	34.537	229.303	80.95	1.8	0.042
	1103.10	0.0033	34.536	229.298	80.90	1.4	0.042
G-6 pH=7.638	0.87	0.5028	83.739	416.588	109.75	389.9	—
	23.05	0.2687	83.505	415.423	109.41	207.5	71.350
	94.75	0.0944	83.330	414.556	96.00	72.8	18.312
	168.08	0.0290	83.265	414.231	86.02	22.4	7.007
	263.43	0.0087	83.245	414.130	82.29	6.7	1.702
	457.77	0.0033	83.239	414.103	81.12	2.5	0.220
	599.73	0.0022	83.238	414.098	80.82	1.7	0.059
	767.58	0.0019	83.238	414.096	80.76	1.5	0.017
	935.35	0.0014	83.237	414.094	80.74	1.1	0.021
	1103.17	0.0012	83.237	414.093	80.71	—	—

Table 2: Evolution of solution chemistry of growth experiments. [Fe(II)] measured via ICP-MS, the initial DIC determined from added NaHCO_3 powder, whereas the subsequent evolutions of DIC, $[\text{CO}_3^{2-}]$, BET-surface area, and solution saturation are calculated via methods detailed in Supplementary information and Section. 3.2.3. Change in ionic strength due to siderite growth is $\lesssim 1\%$. Growth rates between the designed [Fe(II)] and the first measurement are discarded.

$I = 0.175$ molal; $T = 298.15$ K and 1 bar						
Ex.No	Time h	[Fe(II)] molal $\times 10^3$	[DIC] molal $\times 10^3$	[CO ₃ ²⁻] molal $\times 10^6$	Ω	Secondary growth rate mol·m ⁻² ·s ⁻¹ $\times 10^{12}$
RP-1 pH=7.478	1.03	0.1005	6.433	21.807	4.1	—
	23.27	0.1767	6.510	22.066	7.3	—
	95.00	0.1640	6.497	22.023	6.7	0.948
	168.18	0.1432	6.476	21.952	5.8	1.523
	263.63	0.1205	6.453	21.875	4.9	1.269
	457.97	0.0932	6.426	21.783	3.8	0.750
	600.03	0.0803	6.413	21.739	3.3	0.481
	767.87	0.0736	6.407	21.716	3.0	0.213
	935.47	0.0687	6.402	21.700	2.8	0.155
	1103.28	0.0629	6.396	21.680	2.5	0.185
RP-2 pH=7.496	1.03	0.0484	20.075	71.073	6.4	—
	23.27	0.0729	20.099	71.160	9.7	—
	95.00	0.0543	20.081	71.094	7.2	1.391
	168.15	0.0405	20.067	71.045	5.4	1.005
	263.60	0.0324	20.059	71.016	4.3	0.454
	457.97	0.0233	20.050	70.984	3.1	0.249
	600.00	0.0205	20.047	70.974	2.7	0.107
	767.83	0.0179	20.044	70.965	2.4	0.081
	935.43	0.0162	20.043	70.959	2.1	0.055
	1103.25	0.0150	20.041	70.955	2.0	0.037
RP-3 pH=7.770	1.03	0.0405	11.077	75.294	5.7	—
	23.27	0.0654	11.102	75.464	8.2	—
	95.00	0.0549	11.091	75.392	7.7	0.789
	168.20	0.0423	11.079	75.307	5.9	0.914
	263.65	0.0351	11.072	75.258	4.9	0.402
	457.97	0.0260	11.062	75.195	3.6	0.252
	600.05	0.0223	11.059	75.170	3.1	0.138
	767.88	0.0200	11.056	75.155	2.8	0.073
	935.48	0.0203	11.057	75.157	2.8	—
	1103.30	0.0167	11.053	75.133	2.3	0.114
RP-4 pH=7.363	1.03	0.0370	48.310	123.733	8.5	—
	23.27	0.0458	48.319	123.755	10.5	—
	95.00	0.0263	48.299	123.705	6.1	1.453
	169.10	0.0188	48.292	123.686	4.3	0.542
	263.57	0.0140	48.287	123.674	3.2	0.273
	457.97	0.0100	48.283	123.664	2.3	0.109
	599.97	0.0085	48.281	123.660	2.0	0.056
	767.80	0.0075	48.280	123.657	1.7	0.033
	935.40	0.0069	48.280	123.656	1.6	0.020
	1103.22	0.0065	48.279	123.655	1.5	0.013
RP-5 pH=7.742	1.03	0.0245	34.925	222.251	10.1	—
	23.27	0.0347	34.935	222.317	14.4	—
	95.00	0.0202	34.920	222.224	8.3	1.084
	168.17	0.0143	34.915	222.187	5.9	0.429
	263.62	0.0112	34.911	222.167	4.6	0.176
	457.97	0.0074	34.908	222.143	3.1	0.103
	600.02	0.0066	34.907	222.138	2.7	0.032
	767.85	0.0054	34.906	222.130	2.2	0.039
	935.45	0.0054	34.906	222.130	2.2	—
	1103.27	0.0046	34.905	222.125	1.9	0.026
RP-6 pH=7.622	1.03	0.0241	83.476	399.761	17.9	—
	23.27	0.0236	83.475	399.759	17.6	0.108
	95.00	0.0107	83.462	399.697	7.9	0.966
	168.13	0.0070	83.459	399.679	5.2	0.269
	263.58	0.0052	83.457	399.671	3.9	0.101
	457.97	0.0038	83.455	399.664	2.8	0.039
	599.98	0.0035	83.455	399.662	2.6	0.012
	767.82	0.0031	83.455	399.660	2.3	0.013
	935.42	0.0031	83.455	399.661	2.3	—
	1103.23	0.0026	83.454	399.658	1.9	0.015

Table 3: Evolution of solution chemistry (first 46 days) of reprecipitation experiments. Secondary growth rates are normalised against BET-surface area of the seed material (109.75 m²·g⁻¹). DIC and [CO₃²⁻] are calculated as a function of siderite dissolution and precipitation (Supplementary information). Note that siderite dissolution kinetics are excluded from this table.

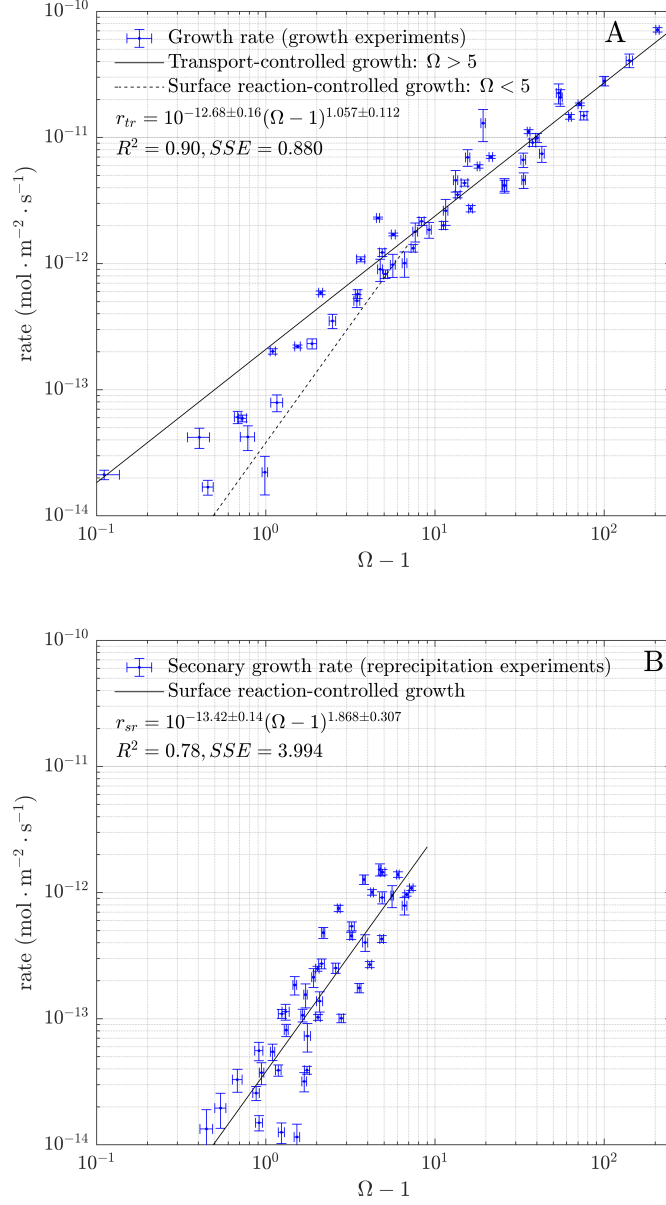


Figure 10: Kinetic data of (A) growth experiments and (B) secondary growth of reprecipitation experiments plotted against supersaturation with respect to siderite. The secondary growth rate (B) is in a good agreement with surface reaction-controlled kinetic behaviour: $r_{sr} \propto (\Omega - 1)^2$. By excluding the deviation at lower supersaturation ($\Omega < 5$; 16 data), the growth experiments (A) are consistent with a transport-controlled kinetic behaviour: $r_{tr} \propto (\Omega - 1)$. Error (3σ) propagation for growth and reprecipitation rate are calculated from $\sigma_d[\text{Fe}^{2+}]$, σ_Ω is based on $\sigma_{[\text{Fe}^{2+}]}$, assuming $\sigma_{[\text{CO}_3^{2-}]} = \sigma_{[\text{Fe}^{2+}]}$, and only considers the uncertainty in calculating Ω at the time of sampling.

among growth by adsorption, at defect sites, and by surface nucleation will require direct microscopic observation employing, for example, atomic force microscopy (Duckworth and Martin 2004; Saldi et al. 2009; Teng et al. 2000). The effect on DIC and Ω during nanocrystalline siderite dissolution is taken into account in the calculations; DIC increase due to dissolution was $\leq 1.2\%$ (Table. 3).

If the kinetic behaviour from the growth experiments at low supersaturation was surface reaction-controlled, by excluding them from fitting (e.g., $\Omega \lesssim 5$; Fig. 10A), a correlation can be obtained that is consistent with a transport-controlled growth rate (r_{tr} ; 37 data):

$$r_{tr} = 10^{-12.68 \pm 0.16} (\Omega - 1)^{1.057 \pm 0.112}, \quad (5)$$

with 95 % confidence bounds, $R^2 = 0.90$, and $SSE = 0.880$. It is important to note that the choice of the cut-off saturation level $\Omega = 5$ is specific to the conditions (temperature, pressure, and ionic strength) and the nature of the siderite seed used in this study.

Transport-controlled kinetic behaviour is subject to the thickness of the diffusive layer, which itself can be a function of fluid dynamics (e.g., stirring speed). Effect of fluid dynamics on transport-controlled kinetic behaviour has been discussed in detail by Mullin (1972), Nielsen (1964, 1984), Plummer et al. (1979) and Watkins et al. (2017). Nielsen (1964, 1984) and Nielsen and Toft (1984) argued that for crystals smaller than $\approx 5\ \mu\text{m}$ (siderite seeds in this study are predominantly $\approx 2\ \mu\text{m}$ spherical particles; Section. 3.2.2), the thickness of the diffusive layer is apparently independent of stirring speed; such small particles are carried with the solution and they sediment so slowly that the liquid flow over their surface is too weak to influence diffusion rate. Stirring speed was not examined as a variable here, but experiments were gently agitated twice a day. We therefore predict little to no dependence of growth rates on stirring speed.

4.3 Comparison with previous siderite kinetic studies

A number of studies have conducted siderite precipitation experiments at surface temperature, with the purpose of deriving siderite solubility (Greenberg and Tomson 1992; Jensen et al. 2002; Singer and Stumm 1970), constraining isotopic fractionation (Dijk et al. 2018; Jimenez-Lopez and Romanek 2004; Wiesli et al. 2004), understanding trace metal incorporation (Romanek et al. 2009), and the recent efforts in characterising the amorphous Fe(II) carbonate precursor (AFC) and its subsequent mineralisation pathways (Azoulay et al. 2012; Dideriksen et al. 2015; Jiang and Tosca 2019; Montes-Hernandez and Renard 2016; Sel et al. 2012). To our knowledge, only Jimenez-Lopez and Romanek (2004) provided the necessary constraints on experimental conditions for a direct comparison of growth kinetics at 25 °C. Jimenez-Lopez and Romanek (2004) conducted two sets of experiments, (1) closed-system/free-drifting syntheses and (2) controlled-chemistry experiments where a constant

chemical condition was maintained by an autotitrator. They reported multiple metastable precursor phases in their harvested solids, and as the important roles of AFC and chukanovite were not known at the time, they chose to report only the precipitation rate of samples that contained $> 50\%$ siderite (determined by XRD). The mixture of multiple phases may have led to the scattering of kinetic data when plotted against supersaturation with respect to pure siderite. This can be demonstrated by refitting their results with the speciation scheme used in this study (Fig. 11). Importantly, our kinetic data are 2 orders of magnitude lower than those reported by Jimenez-Lopez and Romanek (2004) at a comparable supersaturation.

There are a number of factors behind this discrepancy. First, the reported mixtures of multiple phases indicate that the high supersaturation in Jimenez-Lopez and Romanek (2004) experiments might have surpassed and perhaps maintained above the critical supersaturation threshold for homogeneous AFC nucleation (Fig. 2; Jiang and Tosca 2019). If so, two or more mineralisation processes may have withdrawn solution $[\text{Fe(II)}]$, from which the precipitation rate was calculated by Jimenez-Lopez and Romanek (2004). Secondly, the siderite seed used in their study were crystalline siderite with a BET-surface area of $\leq 1.86 \text{ m}^2\cdot\text{g}^{-1}$ (where rates were calculated), compared to the $109.75 \text{ m}^2\cdot\text{g}^{-1}$ of the synthetic seeds used in this study. Aside from the difference in the surface area, the surface activation energy between crystalline and nanocrystalline siderite seeds are no doubt different. Unfortunately, there is insufficient information to conduct a numerical comparison between the surface activation energy of the siderite seed between this investigation and theirs.

Siderite precipitation kinetics has been a core interest of corrosion sciences, particularly concerning the corrosion of mild steel in carbonated media (e.g., Barker et al. 2018; Burkle et al. 2017; Johnson and Tomson 1991; Ma et al. 2018; Saheb et al. 2008, 2010; Sk et al. 2017; Sun and Nešić 2008). Though focused on elevated temperature, multiple studies reported transport-controlled kinetic behaviour across a wide range of physico-chemical conditions (Ma et al. 2018; Sk et al. 2017; Sun and Nešić 2008). For example, Ma et al. (2018) carefully conducted a series of siderite precipitation experiments at a temperature range of $50\text{--}80^\circ\text{C}$, in which the growth of siderite was measured as weight-gain on an electrochemical quartz crystal micro-balance coated with either $\approx 1 \mu\text{m}$ of iron or $\approx 0.5 \mu\text{m}$ of gold. The *in-situ* micro-balance allowed real-time recording of solid mass on the coated quartz plate, enabled Ma et al. (2018) to differentiate between the initial surface nucleation of Fe(II) -carbonates on the coated plate and the continued growth of the nuclei. They fitted the growth rate to a temperature- and surface activation energy-dependent kinetic model originally proposed by Johnson and Tomson (1991) and modified by Sun and Nešić (2008):

$$\text{rate} = k_r e^{-\frac{\Delta G_a}{RT}} K_{sp,T,I}(\Omega - 1), \quad (6)$$

where k_r is kinetic constant: $3.32 \times 10^7 \text{ m}^4\cdot\text{mol}^{-1}\cdot\text{s}^{-1}$, ΔG_a is surface activation energy for growth on siderite nuclei: $73739 \text{ J}\cdot\text{mol}^{-1}$, R is the gas constant $8.314 \text{ J}\cdot\text{mol}^{-1}\cdot\text{K}^{-1}$. In the Ma et al. (2018) model, solution saturation (Ω) with respect to siderite is calculated as the product of concentrations instead

of activities, and the effects of temperature (T ; in K) and stoichiometric ionic strength (I) are taken into account in the solubility product $K_{sp,T,I}$ in the following empirical equation summarised by Sun et al. (2009):

$$\log K_{sp,T,I} = -59.3498 - 0.041377T - \frac{2.196}{T} + 24.5724 \log T + 2.518\sqrt{I} - 0.657I. \quad (7)$$

It should be noted that the temperature-dependent terms in Eq. 7 are based on the relationship proposed by Greenberg and Tomson (1992, and Eq. 2 therein), and the stoichiometric ionic strength-dependent terms are taken from Silva et al. (2002), with the constant in Eq. 7 modified to fit with the average of selected siderite solubility values. The average solubility value concluded by Sun et al. (2009) is identical to the crystalline siderite solubility proposed by Nordstrom et al. (1990): $\log K_{sp,T,I} = -10.89$ at 298.15 K and $I = 0$ molal. This value, in fact, was based on the dissolution experiments conducted by Smith (1918), refitted with a speciation scheme that included FeHCO^{3+} , $\text{FeCO}_3(aq)$, and FeOH^+ (Nordstrom et al. 1990). The apparent concordance reached between Greenberg and Tomson (1992) and Nordstrom et al. (1990) can be partially attributed to the adaptation of speciation scheme and equilibrium constants from the latter by the former. In fact, Nordstrom et al. (1990) also proposed $\log K_{sp} = -10.45$ for precipitated siderite solubility, refitted from the work by Singer and Stumm (1970); a more suitable value for siderite precipitation experiments but nevertheless not used. We, therefore, reason that the difference between siderite solubility calculated from Eq. 7 and the value adopted in this study is largely an artefact between calculation schemes instead of a matter of accuracy.

Because this study considers the effect of stoichiometric ionic strength in the calculation of solution saturation and adopts a basic speciation scheme (no Fe(II)-compound; Supplementary information. S.1), we may implement the temperature dependence proposed by Greenberg and Tomson (1992), and modify the constant to yield a $\log K_{sp} = -10.24$ at 298.15 K:

$$\log K_{sp,T} = -58.6989 - 0.041377T - \frac{2.196}{T} + 24.5724 \log T.$$

In so doing, the kinetic model by Ma et al. (2018) (Eq. 6) and Sun and Nešić (2008) can be extrapolated to 298.15 K for comparison (Fig. 11). Note that a different temperature dependence has been proposed by Bénézech et al. (2009) for temperature range of 25–250 °C, but the difference in the temperature range of 25–80 °C from that of Greenberg and Tomson (1992) is minor.

The similarity between our kinetic data and that extrapolated from Ma et al. (2018) and Sun and Nešić (2008) does not extend beyond the transport-controlled growth kinetic behaviour (linear correlation with supersaturation); our results are more than 2 orders of magnitude higher than the extrapolated constraints (Fig. 11). This exercise underscores the need for more thermodynamic and kinetic data between 25 °C and 80 °C. For example, Stefánsson et

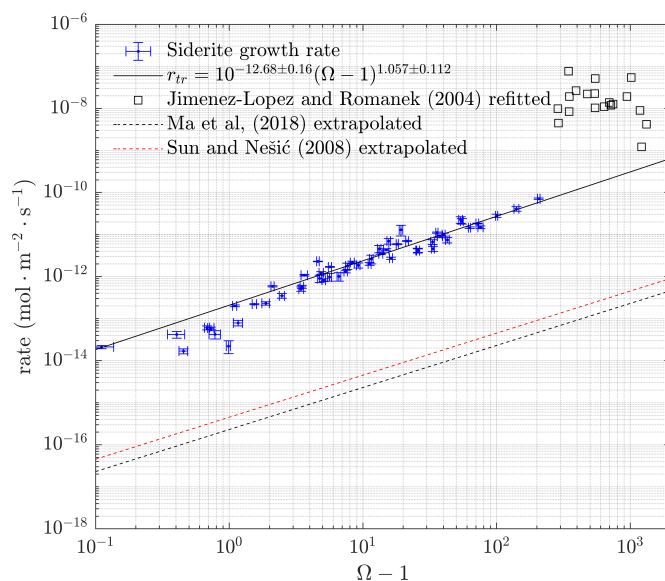


Figure 11: Comparison of siderite growth rates with previous kinetic studies. Jimenez-Lopez and Romanek (2004) experimental results at 25 °C are refitted with the speciation scheme used in this study (squares), ionic strength correction is calculated based on their measured $[\text{Fe}^{2+}]$, pH, and alkalinity. Ma et al. (2018) and Sun and Nešić (2008) used same kinetic model based on high-temperature experiments, and are both extrapolated to 25 °C using the temperature corrections provided in their models (dashed lines).

al. (2013) demonstrated the importance of $\text{NaCO}_3^-(aq)$ and $\text{NaHCO}_3(aq)$ complexes in carbonate speciation at elevated temperature. Not including these carbonate species in high-temperature experiments might have led to overestimations of solution saturation with respect to siderite, thus, potentially contributing to underestimations of kinetic behaviour when extrapolated to 25 °C.

4.4 Comparison with Ca- and Mg-carbonate growth

To compare siderite growth kinetics with the well-documented process of calcite precipitation, calcite growth kinetics are refitted from a comprehensive investigation by Busenberg and Plummer (1986, and Table. 10 therein) at 25 °C in solutions stirred at 260 revolutions per minute (RPM). Busenberg and Plummer (1986) recognised two distinct precipitation regions of calcite (*cal*): (1) near-equilibrium, where growth rate is very low and (2) from $\Omega_{cal} = 1.45$ and higher, where growth rate is proportional to the activity product of dissolved species (Fig. 12A; a similar conclusion was reached in a review by Shiraki and Brantley 1995).

In inhibitor-free aqueous conditions at surface temperature and pressure, the growth rate of siderite is nearly 7-orders of magnitude slower than that of

calcite at their respective supersaturation (Fig. 12B). If extrapolated from the observed transport-controlled kinetic behaviour (Eq. 5), for siderite to achieve a comparable growth rate with that of calcite near-equilibrium, Ω_{sid} needs to exceed 10^5 (Fig. 12B). Such a supersaturated condition is unrealistic in a natural system, as it is far above the critical supersaturation for homogeneous nucleation of precursor AFC phase ($\Omega_{sid} \approx 600$; Jiang and Tosca 2019); pervasive and rapid nucleation of AFC acts as a ceiling for the maximum solution saturation in a natural system.

The significant difference in calcite and siderite growth kinetics has been attributed to the difference in the average surface charge density of Fe^{2+} versus Ca^{2+} (Jimenez-Lopez and Romanek 2004). Due to the smaller ionic radius of Fe^{2+} (0.078 nm) than that of Ca^{2+} (0.1 nm; ionic radii taken from Marcus 1988), a higher activation energy is required to dehydrate the more densely charged Fe^{2+} ion on the crystal surface to form siderite—which can also be conceptualised as a lower dehydration frequency (e.g., Nielsen 1984) or a lower exchange rate of the solvation shell (e.g., Pokrovsky and Schott 2002) associated with smaller cations.

If cation charge density is the main contributor behind the slower growth rate of siderite compared to calcite, one may speculate an even slower growth rate of magnesite (MgCO_3) due to the even lower dehydration frequency of Mg^{2+} (0.072 nm) (Nielsen 1984; Pokrovsky and Schott 2002). Indeed, it has long been hypothesised that high dehydration energy for Mg^{2+} prohibits the formation of magnesite at surface conditions (e.g., Christ and Hostetler 1970; Kowacz et al. 2007; Sayles and Fyfe 1973). Instead, low-temperature Mg-carbonate precipitation involves the formation of metastable nesquehonite ($\text{MgCO}_3 \cdot 3\text{H}_2\text{O}$) and hydromagnesite ($\text{Mg}_5(\text{CO}_3)_4(\text{OH})_2 \cdot 4\text{H}_2\text{O}$).

Abiotic magnesite growth kinetics have only been documented from high-temperature experiments, and the most complete data set to date (e.g., Saldi 2009; Saldi et al. 2009) indicates the growth behaviour of magnesite is controlled by extremely slow surface reactions that involve the desolvation of Mg^{2+} for Ω_{mag} up to 100 in a temperature range of 80–200 °C. Saldi et al. (2009) presented an experimental investigation employing a self-constructed hydrothermal atomic force microscope, which allowed direct measurements of the microscopic propagation velocity of the 2.7 Å-high monomolecular steps on magnesite crystal surface, as well as the frequencies of new steps generation, both as functions of supersaturation. Their diligent examination demonstrated that at elevated temperature (1) step propagation velocity is linearly proportional to supersaturation ($n = 1$) and (2) step generation show a parabolic correlation with supersaturation that is consistent with spiral growth at screw dislocation ($n = 2$). Based on their estimation of activation energies as a function of temperature, Saldi et al. (2009) concluded that spiral growth mechanism for magnesite is prohibited by the much slower step propagation velocity at 25 °C. As such, despite the importance of magnesite growth kinetics, a comparison with siderite growth can not be achieved through temperature extrapolation alone.

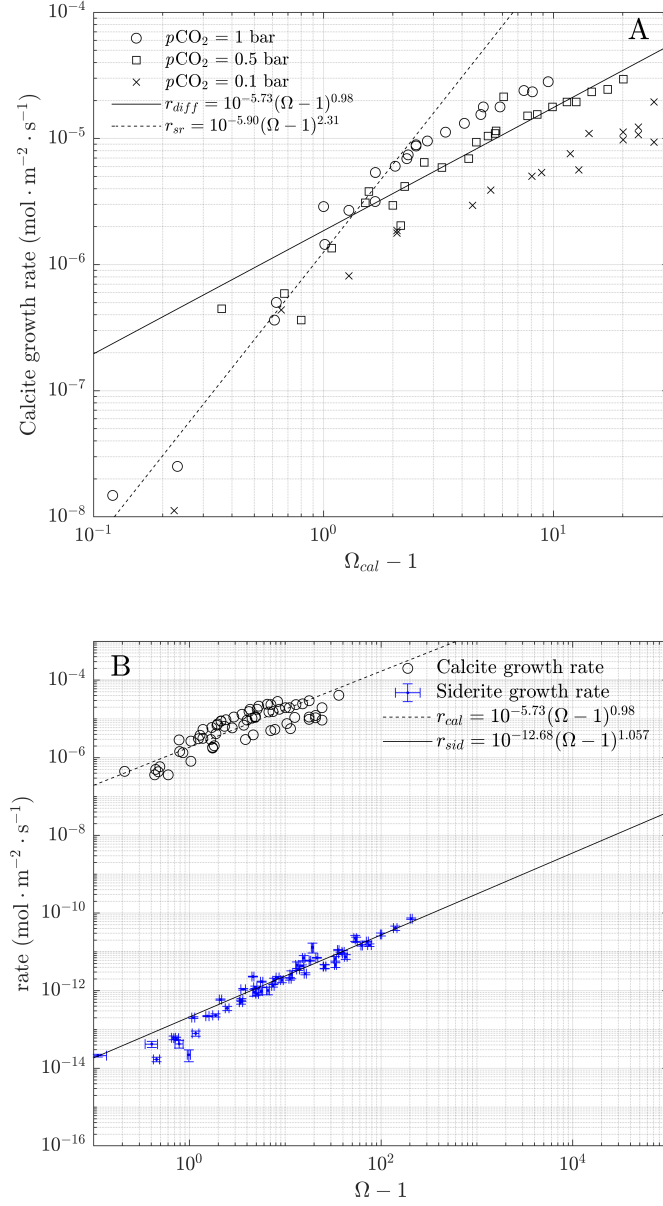


Figure 12: Comparison of growth kinetics between siderite and calcite. (A) Calcite growth kinetics under different $p\text{CO}_2$ levels at 25 °C, recalculated from measurements by Busenberg and Plummer (1986). Though the absolute kinetic behaviours of calcite growth are different under different $p\text{CO}_2$ conditions, two precipitation regions can be identified: a linear correlation with supersaturation at $\Omega_{cal} \gtrsim 2$, but a higher-order correlation near-equilibrium. Exemplary fitted-lines of two separate precipitation regions are plotted for kinetic behaviour under $p\text{CO}_2 = 0.5$ bar. Calcite solubility $\log K_{sp,cal} = -8.48$ (Mucci 1983). (B) Siderite growth rate compared to that of calcite (r_{cal}) (Busenberg and Plummer 1986) at their respective supersaturations.

5 Conclusion

Experimentation on siderite crystal growth at 25 °C yields important constraints on growth kinetics as a function of solution saturation; analogous to calcite growth mechanisms but orders of magnitude slower at comparable saturation. The observed kinetic behaviour of siderite growth is best explained by a chemical affinity-based kinetic model, which predicts a linear correlation with supersaturation ($\Omega - 1$) for growth controlled by transport of dissolved species from the parent solution to the surface fluid (Eq. 5), and a parabolic for growth controlled by spiral mechanism-dominated surface reactions (Eq. 4). Though the differentiation between these two kinetic behaviours with respect to supersaturation is likely sample- and condition-specific, it lays the foundation for further theoretical and experimental exploration on the kinetic isotope fractionation and trace element incorporation during the precipitation of Fe(II)-carbonates; especially in light of the growing understanding of the thermodynamic properties and mineralisation pathways of this group of carbonates.

The slow kinetics of siderite growth explains the commonly reported siderite supersaturation in anoxic water bodies that are either (1) lacking a suitable surface for heterogeneous siderite precipitation, or (2) open-systems with influxes of Fe(II). In the absence of a suitable surface, siderite precipitates via homogeneous nucleation of the precursor phase amorphous Fe(II) carbonate, where solution saturation has to surpass a critical threshold that is significantly higher than siderite equilibrium solubility (Fig. 2; Jiang and Tosca 2019). Because the near-equilibrium growth rate of siderite is extremely slow, any Fe(II) influxes (e.g., microbial Fe(III) reduction, hydrothermal activity, or dissolution of other Fe(II)-minerals) would outpace the slow growth of siderite and lead to the accumulation of Fe^{2+} in the solution, which in turn, increases the solution saturation. This is expected to continue until solution saturation builds to support an appreciable growth/nucleation rate (at high Ω) that balances the Fe(II) influx. In this light, siderite precipitation may be more dynamic and episodic than previously understood, potentially involving multiple mineralisation pathways if nucleation barriers are crossed. This knowledge has important implications for engineering efforts in wetland management, steel corrosion, carbon capture and storage, and long-term nuclear waste storage plan.

Further experimentation is, of course, pivotal in filling the knowledge gap between low- and high-temperature precipitation kinetics and differentiating different surface reaction mechanisms. A complete kinetic framework for Fe(II)-carbonate precipitation holds the key to the genesis of the siderite-rich sedimentary rocks that are fundamental to our understanding of the biogeochemical evolution in the distant past (e.g., Beukes and Gutzmer 2008; Jiang and Tosca 2019; Raiswell et al. 2011; Rasmussen and Muhling 2018; Tosca et al. 2019). More importantly, such knowledge will make a crucial contribution to the Mars 2020 Mission, where the rover will land at Jezero Crater—the only regionally expansive Fe(II)-Mg-carbonate deposit on Mars (Bridges et al.

2018; Wray et al. 2016)—and study these sedimentary formations *in-situ*. Our
interpretations of the mineralogical observations from more than 54 million
kilometres away, however, will be hindered by the lack of kinetic constraints.

770 Acknowledgement

771 The authors thank Chris Romanek and two anonymous reviewers for thought-
772 ful and constructive comments, and Chen Zhu and Jeffrey G. Catalano for edit-
773 orial handling. The authors acknowledge support from NERC grant (NE/M013014/1)
774 and the Leverhulme Trust (PLP-2015-286) to NJT. The authors thank Phil
775 Holdship (Earth Sciences, University of Oxford) for conducting ICP-MS ana-
776 lysis, Robert Jacobs (Chemistry, University of Oxford) for performing BET-
777 surface area analysis, Katherine Clayton (Earth Sciences) for directing XRD
778 analysis, and Jon Wade (Earth Sciences) for assistance with SEM character-
779 isation. CZJ would like to extend appreciation towards Ben Tutolo (Earth Sci-
780 ences, University of Calgary), Ritwika Sengupta, Sascha Holland, and Raphael
781 Pietzsch for in-depth discussions, and to express gratitude towards Sam B.
782 Cornish, Tomas Jonathan, and Helene Asbjørnsen for substantial assistance in
783 Matlab coding and data processing.

References

- Aagaard, P. and H. C. Helgeson (Mar. 1982). ‘Thermodynamic and kinetic constraints on reaction rates among minerals and aqueous solutions; I, Theoretical considerations’. In: *American Journal of Science* 282.3, pp. 237–285. ISSN: 0002-9599. DOI: 10.2475/ajs.282.3.237.
- Azoulay, I., C. Rémazeilles and Ph Refait (May 2012). ‘Determination of standard Gibbs free energy of formation of chukanovite and Pourbaix diagrams of iron in carbonated media’. In: *Corrosion Science* 58, pp. 229–236. ISSN: 0010938X. DOI: 10.1016/j.corsci.2012.01.033.
- Bachan, Aviv and Lee R. Kump (2015). ‘The rise of oxygen and siderite oxidation during the Lomagundi Event’. In: *Proceedings of the National Academy of Sciences* 112.21, pp. 6562–6567. ISSN: 0027-8424. DOI: 10.1073/pnas.1422319112.
- Barker, Richard, Daniel Burkle, Thibaut Charpentier, Harvey Thompson and Anne Neville (Sept. 2018). ‘A review of iron carbonate (FeCO₃) formation in the oil and gas industry’. In: *Corrosion Science* 142.July, pp. 312–341. ISSN: 0010938X. DOI: 10.1016/j.corsci.2018.07.021.
- Bénézech, P., J.L. Dandurand and J.C. Harichoury (July 2009). ‘Solubility product of siderite (FeCO₃) as a function of temperature (25–250 °C)’. In: *Chemical Geology* 265.1-2, pp. 3–12. ISSN: 00092541. DOI: 10.1016/j.chemgeo.2009.03.015.
- Beukes, Nj and J Gutzmer (2008). ‘Origin and paleoenvironmental significance of major iron formations at the Archean-Paleoproterozoic boundary’. In: *Society of Economic Geologists Reviews* 15.August 2016, pp. 5–47. ISSN: 07410123. DOI: 10.5382/Rev.15.01.
- Bridges, John C., Leon J. Hicks and Allan H. Treiman (2018). *Carbonates on mars*. Vol. 5. Elsevier Inc., pp. 89–118. ISBN: 9780128041918. DOI: 10.1016/B978-0-12-804191-8.00005-2.
- (2019). ‘Carbonates on Mars’. In: *Volatiles in the Martian Crust*. Elsevier, pp. 89–118. DOI: 10.1016/B978-0-12-804191-8.00005-2.
- Burkle, D., R. De Motte, W. Taleb, A. Kleppe, T. Comyn, S.M. Vargas, A. Neville and R. Barker (Nov. 2017). ‘In situ SR-XRD study of FeCO₃ precipitation kinetics onto carbon steel in CO₂-containing environments: The influence of brine pH’. In: *Electrochimica Acta* 255, pp. 127–144. ISSN: 00134686. DOI: 10.1016/j.electacta.2017.09.138.
- Burton, W. K., N. Cabrera and F. C. Frank (June 1951). ‘The Growth of Crystals and the Equilibrium Structure of their Surfaces’. In: *Philosophical Transactions of the Royal Society A: Mathematical, Physical and Engineering Sciences* 243.866, pp. 299–358. ISSN: 1364-503X. DOI: 10.1098/rsta.1951.0006.
- Busenberg, E. and L. N. Plummer (1986). ‘A comparative study of the dissolution and crystal growth kinetics of calcite and aragonite’. In: *Studies in Diagenesis, U.S. Geological Survey Bulletin 1578* January 1986, pp. 139–168. ISSN: 00831093.

- Butler, James Newton (1964). *Ionic Equilibrium: A Mathematical Approach*. Reading MA: Addison-Wesley Pub. Co., p. 547.
- Callow, Ben, Ismael Falcon-Suarez, Sharif Ahmed and Juerg Matter (Mar. 2018). ‘Assessing the carbon sequestration potential of basalt using X-ray micro-CT and rock mechanics’. In: *International Journal of Greenhouse Gas Control* 70.December 2017, pp. 146–156. ISSN: 17505836. DOI: 10.1016/j.ijggc.2017.12.008.
- Christ, C. L. and P. B. Hostetler (May 1970). ‘Studies in the system MgO-SiO₂-CO₂-H₂O (II); the activity-product constant of magnesite’. In: *American Journal of Science* 268.5, pp. 439–453. ISSN: 0002-9599. DOI: 10.2475/ajs.268.5.439.
- Christoffersen, Jørgen and Margaret R. Christoffersen (1992). ‘A revised theory for the growth of crystals by surface nucleation’. In: *Journal of Crystal Growth* 121.4, pp. 608–616. ISSN: 00220248. DOI: 10.1016/0022-0248(92)90568-4.
- DePaolo, Donald J. (Feb. 2011). ‘Surface kinetic model for isotopic and trace element fractionation during precipitation of calcite from aqueous solutions’. In: *Geochimica et Cosmochimica Acta* 75.4, pp. 1039–1056. ISSN: 00167037. DOI: 10.1016/j.gca.2010.11.020.
- Dideriksen, Knud, Cathrine Frandsen, Nicolas Bovet, Adam F. Wallace, Ozlem Sel, Tyler Arbour, Alexandra Navrotsky, James J. De Yoreo and Jillian F. Banfield (Sept. 2015). ‘Formation and transformation of a short range ordered iron carbonate precursor’. In: *Geochimica et Cosmochimica Acta* 164, pp. 94–109. ISSN: 00167037. DOI: 10.1016/j.gca.2015.05.005.
- Dijk, Joep van, Alvaro Fernandez, Inigo A. Müller, Mark Lever and Stefano M. Bernasconi (Jan. 2018). ‘Oxygen isotope fractionation in the siderite-water system between 8.5 and 62 °C’. In: *Geochimica et Cosmochimica Acta* 220, pp. 535–551. ISSN: 00167037. DOI: 10.1016/j.gca.2017.10.009.
- Duckworth, Owen W. and Scot T. Martin (2004). ‘Role of molecular oxygen in the dissolution of siderite and rhodochrosite’. In: *Geochimica et Cosmochimica Acta* 68.3, pp. 607–621. ISSN: 00167037. DOI: 10.1016/S0016-7037(00)00464-2.
- Gislason, Sigurdur Reynir et al. (May 2010). ‘Mineral sequestration of carbon dioxide in basalt: A pre-injection overview of the CarbFix project’. In: *International Journal of Greenhouse Gas Control* 4.3, pp. 537–545. ISSN: 17505836. DOI: 10.1016/j.ijggc.2009.11.013.
- Greenberg, Janet and Mason Tomson (Mar. 1992). ‘Precipitation and dissolution kinetics and equilibria of aqueous ferrous carbonate vs temperature’. In: *Applied Geochemistry* 7.2, pp. 185–190. ISSN: 08832927. DOI: 10.1016/0883-2927(92)90036-3.
- Heimann, Adriana, Clark M. Johnson, Brian L. Beard, John W. Valley, Eric E. Roden, Michael J. Spicuzza and Nicolas J. Beukes (May 2010). ‘Fe, C, and O isotope compositions of banded iron formation carbonates demonstrate a major role for dissimilatory iron reduction in ~2.5Ga marine environments’. In: *Earth and Planetary Science Letters* 294.1-2, pp. 8–18. ISSN: 0012821X. DOI: 10.1016/j.epsl.2010.02.015.

- Hillig, W.B. (Dec. 1966). ‘A derivation of classical two-dimensional nucleation kinetics and the associated crystal growth laws’. In: *Acta Metallurgica* 14.12, pp. 1868–1869. ISSN: 00016160. DOI: 10.1016/0001-6160(66)90046-0.
- Holland, H.D. (2007). ‘The Geologic History of Seawater’. In: *Treatise on Geochemistry*. Vol. 6. Elsevier, pp. 1–46. ISBN: 0-08-043751-6. DOI: 10.1016/B0-08-043751-6/06122-3.
- Holland, Heinrich D. (1984). *The Chemical Evolution of the Atmosphere and Oceans*. Princeton: Princeton University Press, p. 598.
- House, William A. (1981). ‘Kinetics of crystallisation of calcite from calcium bicarbonate solutions’. In: *Journal of the Chemical Society, Faraday Transactions 1: Physical Chemistry in Condensed Phases* 77.2, pp. 341–359. ISSN: 03009599. DOI: 10.1039/F19817700341.
- Jensen, Dorte L, Jens K Boddum, Jens Christian Tjell and Thomas H Christensen (Apr. 2002). ‘The solubility of rhodochrosite (MnCO₃) and siderite (FeCO₃) in anaerobic aquatic environments’. In: *Applied Geochemistry* 17.4, pp. 503–511. ISSN: 08832927. DOI: 10.1016/S0883-2927(01)00118-4.
- Jiang, Clancy Zhijian and Nicholas J. Tosca (Jan. 2019). ‘Fe(II)-carbonate precipitation kinetics and the chemistry of anoxic ferruginous seawater’. In: *Earth and Planetary Science Letters* 506, pp. 231–242. ISSN: 0012821X. DOI: 10.1016/j.epsl.2018.11.010.
- Jimenez-Lopez, Concepción and Christopher S. Romanek (Feb. 2004). ‘Precipitation kinetics and carbon isotope partitioning of inorganic siderite at 25°C and 1 atm’. In: *Geochimica et Cosmochimica Acta* 68.3, pp. 557–571. ISSN: 00167037. DOI: 10.1016/S0016-7037(03)00460-5.
- Johnson, M.L. and M.B. Tomson (1991). ‘Ferrous Carbonate Precipitation Kinetics and its Impact CO₂ Corrosion’. In: *CORROSION* Houston, T, p. 268.
- Kandegedara, Ashoka and David B. Rorabacher (Aug. 1999). ‘Noncomplexing Tertiary Amines as “Better” Buffers Covering the Range of pH 3-11. Temperature Dependence of Their Acid Dissociation Constants.’ In: *Analytical Chemistry* 71.15, pp. 3140–3144. ISSN: 0003-2700. DOI: 10.1021/ac9902594.
- Kaufman, Alan J., J.M. Hayes and C. Klein (Dec. 1990). ‘Primary and diagenetic controls of isotopic compositions of iron-formation carbonates’. In: *Geochimica et Cosmochimica Acta* 54.12, pp. 3461–3473. ISSN: 00167037. DOI: 10.1016/0016-7037(90)90298-Y.
- Klein, Cornelis (Oct. 2005). ‘Some Precambrian banded iron-formations (BIFs) from around the world: Their age, geologic setting, mineralogy, metamorphism, geochemistry, and origin’. In: *American Mineralogist* 90.10, pp. 1473–1499. ISSN: 0003004X. DOI: 10.2138/am.2005.1871.
- Kowacz, M., C.V. Putnis and A. Putnis (Nov. 2007). ‘The effect of cation:anion ratio in solution on the mechanism of barite growth at constant supersaturation: Role of the desolvation process on the growth kinetics’. In: *Geochimica et Cosmochimica Acta* 71.21, pp. 5168–5179. ISSN: 00167037. DOI: 10.1016/j.gca.2007.09.008.

- 920 Lasaga, Antonio C. (June 1984). ‘Chemical kinetics of water-rock interactions’.
921 In: *Journal of Geophysical Research: Solid Earth* 89.B6, pp. 4009–4025.
922 ISSN: 01480227. DOI: 10.1029/JB089iB06p04009.
- 923 — (1998). ‘7. Theory of Crystal Growth and Dissolution’. In: *Kinetic Theory in*
924 *the Earth Sciences*. Ed. by H.D. Holland. Princeton: Princeton University
925 Press, pp. 581–618. ISBN: 0-691-03748-5.
- 926 Ma, Zheng, Yang Yang, Bruce Brown, Srdjan Nesic and Marc Singer (Aug.
927 2018). ‘Investigation of precipitation kinetics of FeCO₃ by EQCM’. In:
928 *Corrosion Science* 141.June, pp. 195–202. ISSN: 0010938X. DOI: 10.1016/
929 j.corsci.2018.06.017.
- 930 Marcus, Yizhak (1988). ‘Ionic Radii in Aqueous Solutions’. In: *Chemical Re-*
931 *views* 88, pp. 1475–1498. ISSN: 00959782. DOI: 10.1007/BF00646201. arXiv:
932 1402.6991v1.
- 933 Montes-Hernandez, German and François Renard (Dec. 2016). ‘Time-Resolved
934 in Situ Raman Spectroscopy of the Nucleation and Growth of Siderite, Mag-
935 nesite, and Calcite and Their Precursors’. In: *Crystal Growth and Design*
936 16.12, pp. 7218–7230. ISSN: 15287505. DOI: 10.1021/acs.cgd.6b01406.
- 937 Mucci, A. (Sept. 1983). ‘The solubility of calcite and aragonite in seawater
938 at various salinities, temperatures, and one atmosphere total pressure’. In:
939 *American Journal of Science* 283.7, pp. 780–799. ISSN: 0002-9599. DOI:
940 10.2475/ajs.283.7.780.
- 941 Mullin, J W (1972). *Crystallization*. 2nd. London: Butterworths, p. 600. ISBN:
942 0408703490.
- 943 Nancollas, George H. (Jan. 1979). ‘The growth of crystals in solution’. In: *Ad-*
944 *vances in Colloid and Interface Science* 10.1, pp. 215–252. ISSN: 00018686.
945 DOI: 10.1016/0001-8686(79)87007-4.
- 946 Nancollas, George H. and Michael M Reddy (Dec. 1971). ‘The crystallization
947 of calcium carbonate. II. Calcite growth mechanism’. In: *Journal of Colloid*
948 *and Interface Science* 37.4, pp. 824–830. ISSN: 00219797. DOI: 10.1016/
949 0021-9797(71)90363-8.
- 950 Nielsen, Arne Erik (1964). *Kinetics of precipitation*. New York: Pergamon
951 Press.
- 952 — (Jan. 1981). ‘Theory of electrolyte crystal growth. The parabolic rate law’.
953 In: *Pure and Applied Chemistry* 53.11, pp. 2025–2039. ISSN: 1365-3075. DOI:
954 10.1351/pac198153112025.
- 955 — (1983). ‘Precipitates: formation, coprecipitation, and aging.’ In: *Treatise*
956 *on Analytical Chemistry*. Ed. by I. M. Kolthoff and P. J. Elving. Wiley,
957 pp. 269–347.
- 958 — (July 1984). ‘Electrolyte crystal growth mechanisms’. In: *Journal of Crystal*
959 *Growth* 67.2, pp. 289–310. ISSN: 00220248. DOI: 10.1016/0022-0248(84)
960 90189-1.
- 961 Nielsen, Arne Erik and J Christoffersen (1982). ‘The Mechanisms of Chrystal
962 Growth and Dissolution’. In: *Biological Mineralization and Demineraliza-*
963 *tion*. Ed. by G H Nancollas. Berlin, Heidelberg: Springer Berlin Heidelberg,
964 pp. 37–77. ISBN: 978-3-642-68574-3.

- 965 Nielsen, Arne Erik and Jens M. Toft (1984). 'Electrolyte crystal growth kinet-
966 ics'. In: *Journal of Crystal Growth* 67.2, pp. 278–288. ISSN: 00220248. DOI:
967 10.1016/0022-0248(84)90188-X.
- 968 Nordstrom, Darrell Kirk, L. Niel Plummer, Donald Langmuir, Eurybiades
969 Busenberg, Howard M. May, Blair F. Jones and David L. Parkhurst (Dec.
970 1990). 'Revised Chemical Equilibrium Data for Major Water—Mineral Re-
971 actions and Their Limitations'. In: *Chemical Modeling of Aqueous Systems*
972 *II*, pp. 398–413. DOI: 10.1021/bk-1990-0416.ch031.
- 973 Oelkers, E. H., S. R. Gislason and J. Matter (Oct. 2008). 'Mineral Carbonation
974 of CO₂'. In: *Elements* 4.5, pp. 333–337. ISSN: 1811-5209. DOI: 10.2113/
975 gselements.4.5.333.
- 976 Ogundele, G. I. and W. E. White (Feb. 1986). 'Some Observations on Corrosion
977 of Carbon Steel in Aqueous Environments Containing Carbon Dioxide'. In:
978 *CORROSION* 42.2, pp. 71–78. ISSN: 0010-9312. DOI: 10.5006/1.3584888.
- 979 Plummer, L. N., D. L. Parkhurst and T. M. L. Wigley (Mar. 1979). 'Crit-
980 ical Review of the Kinetics of Calcite Dissolution and Precipitation'. In:
981 pp. 537–573. DOI: 10.1021/bk-1979-0093.ch025.
- 982 Pokrovsky, O. S. and J. Schott (2002). 'Surface chemistry and dissolution kinet-
983 ics of divalent metal carbonates'. In: *Environmental Science and Technology*
984 36.3, pp. 426–432. ISSN: 0013936X. DOI: 10.1021/es010925u.
- 985 Raiswell, Rob, Christopher T. Reinhard, Arkadiusz Derkowski, Jeremy Owens,
986 Simon H. Bottrell, Ariel D. Anbar and Timothy W. Lyons (Feb. 2011).
987 'Formation of syngenetic and early diagenetic iron minerals in the late
988 Archean Mt. McRae Shale, Hamersley Basin, Australia: New insights on
989 the patterns, controls and paleoenvironmental implications of authigenic
990 mineral formation'. In: *Geochimica et Cosmochimica Acta* 75.4, pp. 1072–
991 1087. ISSN: 00167037. DOI: 10.1016/j.gca.2010.11.013.
- 992 Rasmussen, Birger and Janet R. Muhling (Mar. 2018). 'Making magnetite late
993 again: Evidence for widespread magnetite growth by thermal decompos-
994 ition of siderite in Hamersley banded iron formations'. In: *Precambrian*
995 *Research* 306.June 2017, pp. 64–93. ISSN: 03019268. DOI: 10.1016/j.
996 precamres.2017.12.017.
- 997 Rimstidt, J.D. and H.L. Barnes (Nov. 1980). 'The kinetics of silica-water re-
998 actions'. In: *Geochimica et Cosmochimica Acta* 44.11, pp. 1683–1699. ISSN:
999 00167037. DOI: 10.1016/0016-7037(80)90220-3.
- 1000 Romanek, Christopher S., Concepción Jiménez-López, Alejandro Rodriguez
1001 Navarro, Monica Sánchez-Román, Nita Sahai and Max Coleman (Sept.
1002 2009). 'Inorganic synthesis of Fe–Ca–Mg carbonates at low temperature'.
1003 In: *Geochimica et Cosmochimica Acta* 73.18, pp. 5361–5376. ISSN: 00167037.
1004 DOI: 10.1016/j.gca.2009.05.065.
- 1005 Saheb, M., D. Neff, Ph Dillmann, H. Matthiesen and E. Foy (Sept. 2008).
1006 'Long-term corrosion behaviour of low-carbon steel in anoxic environment:
1007 Characterisation of archaeological artefacts'. In: *Journal of Nuclear Mater-*
1008 *ials* 379.1-3, pp. 118–123. ISSN: 00223115. DOI: 10.1016/j.jnucmat.2008.
1009 06.019.

- 1010 Saheb, M., M. Descostes, D. Neff, H. Matthiesen, A. Michelin and P. Dillmann
1011 (Dec. 2010). 'Iron corrosion in an anoxic soil: Comparison between thermo-
1012 dynamic modelling and ferrous archaeological artefacts characterised along
1013 with the local in situ geochemical conditions'. In: *Applied Geochemistry*
1014 25.12, pp. 1937–1948. ISSN: 08832927. DOI: 10.1016/j.apgeochem.2010.
1015 10.010.
- 1016 Saldi, Giuseppe (2009). 'Les cinétiques de dissolution et précipitation de la
1017 magnesite aux conditions hydrothermales'. PhD thesis. Thèse de l'Université
1018 Paul-Sabatier, Toulouse, p. 184.
- 1019 Saldi, Giuseppe D., Guntram Jordan, Jacques Schott and Eric H. Oelkers (Oct.
1020 2009). 'Magnesite growth rates as a function of temperature and saturation
1021 state'. In: *Geochimica et Cosmochimica Acta* 73.19, pp. 5646–5657. ISSN:
1022 00167037. DOI: 10.1016/j.gca.2009.06.035.
- 1023 Sayles, F.L. and W.S. Fyfe (Jan. 1973). 'The crystallization of magnesite from
1024 aqueous solution'. In: *Geochimica et Cosmochimica Acta* 37.1, pp. 87–99.
1025 ISSN: 00167037. DOI: 10.1016/0016-7037(73)90246-9.
- 1026 Schwab, A. P. and W. L. Lindsay (1983). 'Effect of Redox on the Solubility
1027 and Availability of Iron'. In: *Soil Science Society of America Journal* 47.2,
1028 p. 201. ISSN: 0361-5995. DOI: 10.2136/sssaj1983.03615995004700020005x.
- 1029 Sel, Ozlem, A.V. Radha, Knud Dideriksen and Alexandra Navrotsky (June
1030 2012). 'Amorphous iron (II) carbonate: Crystallization energetics and com-
1031 parison to other carbonate minerals related to CO₂ sequestration'. In:
1032 *Geochimica et Cosmochimica Acta* 87, pp. 61–68. ISSN: 00167037. DOI:
1033 10.1016/j.gca.2012.03.011.
- 1034 Shiraki, Ryoji and Susan L Brantley (Apr. 1995). 'Kinetics of near-equilibrium
1035 calcite precipitation at 100°C: An evaluation of elementary reaction-based
1036 and affinity-based rate laws'. In: *Geochimica et Cosmochimica Acta* 59.8,
1037 pp. 1457–1471. ISSN: 00167037. DOI: 10.1016/0016-7037(95)00055-5.
- 1038 Silva, Carlos A R, Xuewu Liu and F J Millero (2002). 'Solubility of Siderite
1039 (FeCO₃) in NaCl Solutions'. In: *Journal of Solution Chemistry* 31.2,
1040 pp. 97–108. ISSN: 0095-9782. DOI: 10.1023/A:1015275618138.
- 1041 Singer, Philip C. and Werner Stumm (Mar. 1970). 'THE SOLUBILITY OF
1042 FERROUS IRON IN CARBONATE-BEARING WATERS'. In: *Journal*
1043 *- American Water Works Association* 62.3, pp. 198–202. ISSN: 0003150X.
1044 DOI: 10.1002/j.1551-8833.1970.tb03888.x.
- 1045 Sk, Mobbassar Hassan, Aboubakr M. Abdullah, Monika Ko, Bridget Ingham,
1046 Nick Laycock, Rakesh Arul and David E. Williams (Sept. 2017). 'Local
1047 supersaturation and the growth of protective scales during CO₂ corrosion
1048 of steel: Effect of pH and solution flow'. In: *Corrosion Science* 126. January,
1049 pp. 26–36. ISSN: 0010938X. DOI: 10.1016/j.corsci.2017.05.026.
- 1050 Smith, Herbert J. (June 1918). 'ON EQUILIBRIUM IN THE SYSTEM: FER-
1051 ROUS CARBONATE, CARBON DIOXIDE AND WATER. 1'. In: *Journal*
1052 *of the American Chemical Society* 40.6, pp. 879–883. ISSN: 0002-7863. DOI:
1053 10.1021/ja02239a002.
- 1054 Stefánsson, Andri, Pascale Bénézech and Jacques Schott (Nov. 2013). 'Car-
1055 bonic acid ionization and the stability of sodium bicarbonate and carbon-

ate ion pairs to 200°C – A potentiometric and spectrophotometric study’. In: *Geochimica et Cosmochimica Acta* 120, pp. 600–611. ISSN: 00167037. DOI: 10.1016/j.gca.2013.04.023.

Sun, W. and S. Nešić (Apr. 2008). ‘Kinetics of Corrosion Layer Formation: Part 1—Iron Carbonate Layers in Carbon Dioxide Corrosion’. In: *CORROSION* 64.4, pp. 334–346. ISSN: 0010-9312. DOI: 10.5006/1.3278477.

Sun, Wei, Srdjan Nešić and Richard C. Woollam (June 2009). ‘The effect of temperature and ionic strength on iron carbonate (FeCO₃) solubility limit’. In: *Corrosion Science* 51.6, pp. 1273–1276. ISSN: 0010938X. DOI: 10.1016/j.corsci.2009.03.009.

Teng, H. Henry, Patricia M. Dove and James J. De Yoreo (July 2000). ‘Kinetics of calcite growth: surface processes and relationships to macroscopic rate laws’. In: *Geochimica et Cosmochimica Acta* 64.13, pp. 2255–2266. ISSN: 00167037. DOI: 10.1016/S0016-7037(00)00341-0.

Tosca, Nicholas J., Clancy Zhijian Jiang, Birger Rasmussen and Janet Muhling (Aug. 2019). ‘Products of the iron cycle on the early Earth’. In: *Free Radical Biology and Medicine* 140. December 2018, pp. 138–153. ISSN: 08915849. DOI: 10.1016/j.freeradbiomed.2019.05.005.

van Cappellen, P (1991). ‘The Formation of Marine Apatite: A Kinetic Study’. PhD thesis. Yale University, p. 240.

van Enckevort, W. J. P., P. Bennema and W. H. van der Linden (Jan. 1981). ‘On the Observation of Growth Spirals with very Low Step Heights on Potash Alum Single Crystals’. In: *Zeitschrift für Physikalische Chemie* 124.2, pp. 171–191. ISSN: 0942-9352. DOI: 10.1524/zpch.1981.124.2.171.

Wajon, Johannes Edmund, Goen-Eng Ho and Peter J. Murphy (Jan. 1985). ‘Rate of precipitation of ferrous iron and formation of mixed iron-calcium carbonates by naturally occurring carbonate materials’. In: *Water Research* 19.7, pp. 831–837. ISSN: 00431354. DOI: 10.1016/0043-1354(85)90140-X.

Watkins, James M., Donald J. DePaolo and E. Bruce Watson (Jan. 2017). ‘Kinetic Fractionation of Non-Traditional Stable Isotopes by Diffusion and Crystal Growth Reactions’. In: *Reviews in Mineralogy and Geochemistry* 82.1, pp. 85–125. ISSN: 1529-6466. DOI: 10.2138/rmg.2017.82.4.

Wiesli, René A., Brian L. Beard and Clark M. Johnson (Nov. 2004). ‘Experimental determination of Fe isotope fractionation between aqueous Fe(II), siderite and “green rust” in abiotic systems’. In: *Chemical Geology* 211.3-4, pp. 343–362. ISSN: 00092541. DOI: 10.1016/j.chemgeo.2004.07.002.

Wray, James J, Scott L Murchie, Janice L Bishop, Bethany L Ehlmann, Ralph E Milliken, Mary Beth Wilhelm, Kimberly D Seelos and Matthew Chojnacki (Apr. 2016). ‘Orbital evidence for more widespread carbonate-bearing rocks on Mars’. In: *Journal of Geophysical Research: Planets* 121.4, pp. 652–677. ISSN: 21699097. DOI: 10.1002/2015JE004972.

Xu, Tianfu, John A. Apps and Karsten Pruess (June 2004). ‘Numerical simulation of CO₂ disposal by mineral trapping in deep aquifers’. In: *Applied Geochemistry* 19.6, pp. 917–936. ISSN: 08832927. DOI: 10.1016/j.apgeochem.2003.11.003.

- 1101 Xu, Tianfu, John A. Apps and Karsten Pruess (Apr. 2005). ‘Mineral sequest-
 1102 ration of carbon dioxide in a sandstone–shale system’. In: *Chemical Geology*
 1103 217.3-4, pp. 295–318. ISSN: 00092541. DOI: 10.1016/j.chemgeo.2004.12.
 1104 015.
- 1105 Zhang, Jingwu and George H. Nancollas (Nov. 1990). ‘Kink densities along a
 1106 crystal surface step at low temperatures and under nonequilibrium condi-
 1107 tions’. In: *Journal of Crystal Growth* 106.2-3, pp. 181–190. ISSN: 00220248.
 1108 DOI: 10.1016/0022-0248(90)90062-P.
- 1109 — (Apr. 1998). ‘Kink Density and Rate of Step Movement during Growth and
 1110 Dissolution of an AB Crystal in a Nonstoichiometric Solution’. In: *Journal*
 1111 *of Colloid and Interface Science* 200.1, pp. 131–145. ISSN: 00219797. DOI:
 1112 10.1006/jcis.1997.5357.

1113 Supplementary information

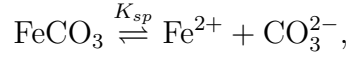
1114 S.1 Thermodynamic calculations

1115 Solution saturation is conventionally expressed as saturation state (Ω) with
1116 respect to a mineral phase in the following form:

$$\Omega = \frac{IAP}{K_{sp}},$$

1117 where K_{sp} is the solubility product of the mineral phase and IAP is the ionic
1118 activity product of the corresponding dissolved ions in the solution. If $\Omega > 1$,
1119 mineral precipitation is predicted, otherwise, dissolution.

1120 Siderite dissolution reaction may be written as follows:



1121 and the IAP of this reaction takes the following form (assuming water activity
1122 of unity and pure mineral phase):

$$IAP = a_{\text{Fe}^{2+}} a_{\text{CO}_3^{2-}},$$

1123 where a_i is the thermodynamic activity of the i th dissolved species, and can
1124 be estimated as a product of its molar concentration (C_i) and its activity
1125 coefficient (γ_i) in a given solution chemistry:

$$a_i = \gamma_i C_i.$$

1126 Approximation of single-ion activity coefficients in a complex, multi-electrolyte
1127 solution is still intensely debated. The most widely adopted approximation
1128 is often one derivative or another of the Debye-Hückel equation (Debye and
1129 Hückel 1923). This study adopts the \dot{B} equation, formulated within the frame-
1130 work of the Helgeson-Kirkham-Flowers model (Helgeson and Kirkham 1974;
1131 Helgeson et al. 1981; Helgeson 1969; Shock et al. 1992; Tanger and Helgeson
1132 1988):

$$\log \gamma_i = -\frac{Az_i^2\sqrt{\bar{I}}}{1 + B\dot{a}_i\sqrt{\bar{I}}} + \dot{B}\bar{I}, \quad (8)$$

1133 where A and B are the molal Debye-Hückel coefficients, z_i is the valency of
1134 the i th ion, \dot{a}_i is the ion size parameter describing the mean distance of the
1135 closest approach of the i th ion, \dot{B} is a temperature-dependent fitting para-
1136 meter, and \bar{I} is the true ionic strength that describes the electrostatic force an
1137 ion experiences from surrounding charged species (all parameters are listed in
1138 Table. 4). The true ionic strength (\bar{I}) differs from the more widely used stoi-
1139 chiometric ionic strength (I) by taking into account the formation of aqueous
1140 compounds/complexes. In other words, at conditions where ion association
1141 is significant, the true ionic strength of a solution may be significantly lower
1142 than the stoichiometric ionic strength. The stoichiometric ionic strength of all

$I = 0.175$ molal; $T = 298.15$ K and 1 bar		
Species	\bar{a} ($\times 10^{-10}$ m)	γ
H^+	9	0.8180
Fe^{2+}	6	0.3501
CO_3^{2-}	4.5	0.3058
HCO_3^-	4.5	0.7529
OH^-	3.5	0.7322
$CO_2(aq)$	4	1.0167
Constants	Values	Sources
A ($kg^{1/2} \cdot mol^{-1/2}$)	0.5039	
B ($kg^{1/2} \cdot mol^{-1/2} \cdot m^{-1}$)	3.2716×10^9	Helgeson and Kirkham (1974)
\bar{B}	0.041	
K_0 (molal \cdot bar $^{-1}$)	3.3×10^{-2}	Sander (2015)
$\log K_1$	-6.1486	Eq. 10
$\log K_2$	-9.8349	Eq. 11
$\log K_{sp}$	-10.24	Singer and Stumm (1970)

Table 4: Thermodynamic properties and constants. Ion size parameter \bar{a} of dissolved species taken from Kielland (1937). Single-ion activity coefficients calculated through \bar{B} equation (Eq. 8).

experiments are fixed at 0.175 molal (including $I_{MOPS} = 0.04$ molal; Buffer Calculator: <http://www.liv.ac.uk/buffers>).

At the conditions and solution concentrations investigated here, the number of Fe(II)-bearing complexes and their abundance are intensely debated and often poorly constrained. For example, many studies include soluble $FeCO_3(aq)$ and $FeHCO_3^+(aq)$ species in their calculations of siderite solubility (e.g., Greenberg and Tomson 1992; Jensen et al. 2002; Ptacek 1992; Silva et al. 2002). Some studies included a number of additional complexes (e.g., $FeOH^+$, $Fe(OH)_2(aq)$, $Fe(OH)_3^-$, $Fe(CO_3)_2^{2-}(aq)$, etc.), but others questioned whether any of these complexes exist at all (e.g., see review by Fosbøl et al. 2010 and experimental examination by Singer and Stumm 1970). The differences in the employed speciation schemes contribute to a wide range of reported values of siderite solubility, from $\log K_{sp} = -10.24$ (Singer and Stumm 1970) to -11.06 (Ptacek 1992) (Table. 5). It is, therefore, important to specify the use of speciation schemes in any discussion and comparison regarding solution saturation and reaction kinetics.

It is worth noting that $NaCO_3^-(aq)$ and $NaHCO_3(aq)$ complexes may become important when extrapolating the kinetic-saturation relationship presented here to elevated temperatures. For example, Stefánsson et al. (2013) experimentally investigated carbonic acid ionisation/dissociation in dilute hydrothermal solutions up to 200 °C. By fitting their measurements on the dissociation constants of carbonic acid to an extended van't Hoff expression (Stefánsson et al. 2013, and Table. 2 & 3 therein), Stefánsson et al. (2013) concluded $NaCO_3^-(aq)$ is important at temperature ≥ 80 °C and $NaHCO_3(aq)$ when ≥ 100 °C.

For maintaining the internal consistency of calculations, and ensuring the kinetic-saturation relations presented here are not dependent on assumptions regarding Fe(II)-speciation, this study adopts a basic speciation scheme with no soluble complex (complete dissociation) and the corresponding siderite solubility $\log K_{sp} = -10.24$ (Singer and Stumm 1970). By assuming complete dissociation, the true ionic strength equates to the stoichiometric ionic strength

$I = 0$ molal, $T = 298.15$ K, and 1 bar, unless noted

$\log K_{sp}$	Method	Speciation scheme	Sources
-10.24	Precipitation		Singer and Stumm (1970)
-10.32 ³	Dissolution (wet)	FeHCO_3^{3+} , $\text{FeCO}_3(aq)$	Jensen et al. (2002)
-10.43 ⁴	Dissolution (wet)	FeHCO_3^{3+} , $\text{FeCO}_3(aq)$	Jensen et al. (2002)
-10.45 ³	Refitting Singer and Stumm (1970)	FeHCO_3^{3+} , $\text{FeCO}_3(aq)$, FeOH^+	Nordstrom et al. (1990)
-10.46 ^{1,2}	Dissolution	$\text{Fe}(\text{HCO}_3)_2(aq)$	Smith (1918)
-10.50 ¹	Refitting Smith (1918)	$\text{Fe}(\text{HCO}_3)_2(aq)$	Kelley and Anderson (1935)
-10.59 ⁵	Refitting Greenberg and Tomson (1992)	$\text{FeCO}_3(aq)$, $\text{Fe}(\text{CO}_3)_2^{2-}$	Preis and Gamsjäger (2002)
-10.68 ³	Dissolution (dry)	FeHCO_3^{3+} , $\text{FeCO}_3(aq)$	Jensen et al. (2002)
-10.68	Refitting Smith (1918)	$\text{Fe}(\text{HCO}_3)_2(aq)$	Kelley and Anderson (1935)
-10.77 ³	Precipitation	FeHCO_3^{3+} , $\text{FeCO}_3(aq)$, FeOH^+	Greenberg and Tomson (1992)
-10.80 ⁵	Dissolution	$\text{FeCO}_3(aq)$, $\text{Fe}(\text{CO}_3)_2^{2-}$	Bruno et al. (1992)
-10.89 ³	"Refitting Smith (1918)	FeHCO_3^{3+} , $\text{FeCO}_3(aq)$, FeOH^+	Nordstrom et al. (1990)
-11.03 ⁴	Dissolution (dry)	FeHCO_3^{3+} , $\text{FeCO}_3(aq)$	Jensen et al. (2002)
-11.06 ³	Dissolution	FeHCO_3^{3+} , $\text{FeCO}_3(aq)$, FeOH^+	Ptacek and Blowes (1993)

Table 5: A shortlist of reported values of siderite solubility product. Speciation scheme section indicates soluble Fe(II)-complex(s) in addition to the basic speciation scheme used in the calculation of solubility product. Note the equilibrium constants can vary significantly for the same Fe(II)-complex, the reader is referred to references provided in the source. (wet) and (dry) differentiate solubility experimentation using freshly precipitated (wet) versus matured crystalline (dry) siderite. ¹: calculated for temperature at 30 °C. ²: no ionic strength control was applied to experiments. ³: equilibrium constants for soluble Fe(II)-complexes from Nordstrom et al. (1990). ⁴: equilibrium constants for soluble Fe(II)-complexes from Fouillac and Criaud (1984). ⁵: equilibrium constants for soluble Fe(II)-complexes from Bruno et al. (1992). It is demonstrated here the disparity in $\log K_{sp}$ can be caused by the differences in the methods of achieving equilibrium, the natures (e.g., wet vs. dry) of materials used, the applied speciation schemes, and the equilibrium constants of Fe(II)-complexes for the same speciation scheme.

of the solution, which can be easily calculated as half the sum of the concentrations (C) times the square of valencies (z) of all dissolved species (Lewis and Randall 1921):

$$\bar{I} \approx I = \frac{1}{2} \sum C_i z_i^2.$$

S.2 Carbonate speciation calculation

Carbonate speciation in the solution is estimated based on the initial dissolved inorganic carbon (DIC; the total amount of NaHCO_3 added; bracketed in Eq. 9), pH, and activity coefficients of all carbonate species (Table. 4). In a simplified form, the $\text{CO}_2(g)$ dissolution and dissociation reactions may be

1182 written as follows:



1183 where the equilibrium constants are equal to:

$$K_0 = \frac{a_{\text{CO}_2(aq)}}{p\text{CO}_2},$$

1184

$$K_1 = \frac{a_{\text{HCO}_3^-} a_{\text{H}^+}}{a_{\text{CO}_2(aq)}},$$

1185

$$K_2 = \frac{a_{\text{CO}_3^{2-}} a_{\text{H}^+}}{a_{\text{HCO}_3^-}},$$

1186 and K_0 is the Henry's law constant of the solubility of $\text{CO}_2(g)$ ($0.033 \text{ molal} \cdot \text{bar}^{-1}$
 1187 at 298.15 K ; Sander 2015); K_1 and K_2 are referred to as the 1st and 2nd disso-
 1188 ciation constants of carbonic acid. The deviation of the dissociation constants
 1189 from their values at $I = 0 \text{ molal}$ (K_1^0 and K_2^0) with increasing solution ionic
 1190 strength can be estimated from the deviation in the activity coefficients of the
 1191 carbonate species:

$$\log K_1 = \log K_1^0 - \log \frac{\gamma_{\text{H}^+} \gamma_{\text{HCO}_3^-}}{\gamma_{\text{CO}_2(aq)}}, \quad (10)$$

1192

$$\log K_2 = \log K_2^0 - \log \frac{\gamma_{\text{H}^+} \gamma_{\text{CO}_3^{2-}}}{\gamma_{\text{HCO}_3^-}}, \quad (11)$$

1193 and $\log K_1^0 = -6.3663$, $\log K_2^0 = -10.3135$, calculated from the Gibbs free
 1194 energy of reactions in Eq. 9, with thermodynamic properties taken from
 1195 CODATA database (Cox et al. 1989).

1196 The $p\text{CO}_2$ and $[\text{CO}_3^{2-}]$ of each experiment can be subsequently calculated
 1197 from solution pH and DIC via the following equations:

$$p\text{CO}_2 = \frac{[\text{H}^+]^2 \text{DIC}}{K_0[\text{H}^+]^2 + K_0 K_1 [\text{H}^+] + K_0 K_1 K_2},$$

1198

$$[\text{CO}_3^{2-}] = \frac{K_1 K_2 \text{DIC}}{[\text{H}^+]^2 + K_1 [\text{H}^+] + K_1 K_2}, \quad (12)$$

1199 or:

$$[\text{CO}_3^{2-}] = \frac{p\text{CO}_2 K_0 K_1 K_2}{[\text{H}^+]^2}.$$

References

- Bruno, Jordi, Paul Wersin and Werner Stumm (1992). 'On the influence of carbonate in mineral dissolution: II. The solubility of $\text{FeCO}_3(\text{s})$ at 25°C and 1 atm total pressure'. In: *Geochimica et Cosmochimica Acta* 56.3, pp. 1149–1155. ISSN: 00167037. DOI: 10.1016/0016-7037(92)90052-K.
- Cox, J. D., Donald D. Wagman and V. A. Medvedev (1989). *CODATA Key Values for Thermodynamics*. Final Repo. Hemisphere Publishing Corporation. ISBN: 0-89116-758-7.
- Debye, P. and E. Hückel (1923). 'The theory of electrolytes I. The lowering of the freezing point and related occurrences'. In: *Physikalische Zeitschrift* 24, pp. 185–206.
- Fosbøl, P. L., K. Thomsen and E. H. Stenby (Apr. 2010). 'Review and recommended thermodynamic properties of FeCO_3 '. In: *Corrosion Engineering, Science and Technology* 45.2, pp. 115–135. ISSN: 1478-422X. DOI: 10.1179/174327808X286437.
- Fouillac, C. and A. Criaud (1984). 'Carbonate and bicarbonate trace metal complexes: Critical reevaluation of stability constants.' In: *GEOCHEMICAL JOURNAL* 18.6, pp. 297–303. ISSN: 0016-7002. DOI: 10.2343/geochemj.18.297.
- Greenberg, Janet and Mason Tomson (Mar. 1992). 'Precipitation and dissolution kinetics and equilibria of aqueous ferrous carbonate vs temperature'. In: *Applied Geochemistry* 7.2, pp. 185–190. ISSN: 08832927. DOI: 10.1016/0883-2927(92)90036-3.
- Helgeson, H. C. and D. H. Kirkham (Dec. 1974). 'Theoretical prediction of the thermodynamic behavior of aqueous electrolytes at high pressures and temperatures; II, Debye-Huckel parameters for activity coefficients and relative partial molal properties'. In: *American Journal of Science* 274.10, pp. 1199–1261. ISSN: 0002-9599. DOI: 10.2475/ajs.274.10.1199. arXiv: 6875208.
- Helgeson, H. C., D. H. Kirkham and G. C. Flowers (Dec. 1981). 'Theoretical prediction of the thermodynamic behavior of aqueous electrolytes by high pressures and temperatures; IV, Calculation of activity coefficients, osmotic coefficients, and apparent molal and standard and relative partial molal properties to 600 d'. In: *American Journal of Science* 281.10, pp. 1249–1516. ISSN: 0002-9599. DOI: 10.2475/ajs.281.10.1249.
- Helgeson, Harold C (Sept. 1969). 'Thermodynamics of hydrothermal systems at elevated temperatures and pressures'. In: *American Journal of Science* 267.7, pp. 729–804. ISSN: 0002-9599. DOI: 10.2475/ajs.267.7.729.
- Jensen, Dorte L, Jens K Boddum, Jens Christian Tjell and Thomas H Christensen (Apr. 2002). 'The solubility of rhodochrosite (MnCO_3) and siderite (FeCO_3) in anaerobic aquatic environments'. In: *Applied Geochemistry* 17.4, pp. 503–511. ISSN: 08832927. DOI: 10.1016/S0883-2927(01)00118-4.
- Kelley, K. K. and C. T. Anderson (1935). 'Contributions to the data on theoretical metallurgy IV: Metal carbonates: correlations and applications of

- thermodynamic properties'. In: *US Department of the Interior, Bureau of Mines* 1-73.
- Kielland, Jacob (Sept. 1937). 'Individual Activity Coefficients of Ions in Aqueous Solutions'. In: *Journal of the American Chemical Society* 59.9, pp. 1675–1678. ISSN: 15205126. DOI: 10.1021/ja01288a032.
- Lewis, Gilbert N. and Merle Randall (May 1921). 'THE ACTIVITY COEFFICIENT OF STRONG ELECTROLYTES. 1'. In: *Journal of the American Chemical Society* 43.5, pp. 1112–1154. ISSN: 0002-7863. DOI: 10.1021/ja01438a014.
- Nordstrom, Darrell Kirk, L. Niel Plummer, Donald Langmuir, Eurybiades Busenberg, Howard M. May, Blair F. Jones and David L. Parkhurst (Dec. 1990). 'Revised Chemical Equilibrium Data for Major Water—Mineral Reactions and Their Limitations'. In: *Chemical Modeling of Aqueous Systems II*, pp. 398–413. DOI: 10.1021/bk-1990-0416.ch031.
- Preis, Wolfgang and Heinz Gamsjäger (2002). 'Critical evaluation of solubility data: Enthalpy of formation of siderite'. In: *Physical Chemistry Chemical Physics* 4.16, pp. 4014–4019. ISSN: 14639076. DOI: 10.1039/b203626f.
- Ptacek, C. J. and David W. Blowes (Dec. 1993). 'Influence of Siderite on the Pore-Water Chemistry of Inactive Mine-Tailings Impoundments'. In: pp. 172–189. DOI: 10.1021/bk-1994-0550.ch013.
- Ptacek, Carol Jane (1992). 'Experimental determination of siderite solubility in high ionic-strength aqueous solutions.' PhD. University of Waterloo, Ontario, Canada.
- Sander, R. (Apr. 2015). 'Compilation of Henry's law constants (version 4.0) for water as solvent'. In: *Atmospheric Chemistry and Physics* 15.8, pp. 4399–4981. ISSN: 1680-7324. DOI: 10.5194/acp-15-4399-2015.
- Shock, Everett L., Eric H. Oelkers, James W. Johnson, Dimitri A. Sverjensky and Harold C. Helgeson (Dec. 1992). 'Calculation of the thermodynamic properties of aqueous species at high pressures and temperatures. Effective electrostatic radii, dissociation constants and standard partial molal properties to 1000 °C and 5 kbar'. In: *J. Chem. Soc., Faraday Trans.* 88.6, pp. 803–826. ISSN: 0956-5000. DOI: 10.1039/FT9928800803.
- Silva, Carlos A R, Xuewu Liu and F J Millero (2002). 'Solubility of Siderite (FeCO_3) in NaCl Solutions'. In: *Journal of Solution Chemistry* 31.2, pp. 97–108. ISSN: 0095-9782. DOI: 10.1023/A:1015275618138.
- Singer, Philip C. and Werner Stumm (Mar. 1970). 'THE SOLUBILITY OF FERROUS IRON IN CARBONATE-BEARING WATERS'. In: *Journal - American Water Works Association* 62.3, pp. 198–202. ISSN: 0003150X. DOI: 10.1002/j.1551-8833.1970.tb03888.x.
- Smith, Herbert J. (June 1918). 'ON EQUILIBRIUM IN THE SYSTEM: FERROUS CARBONATE, CARBON DIOXIDE AND WATER. 1'. In: *Journal of the American Chemical Society* 40.6, pp. 879–883. ISSN: 0002-7863. DOI: 10.1021/ja02239a002.
- Stefánsson, Andri, Pascale Bénézech and Jacques Schott (Nov. 2013). 'Carbonic acid ionization and the stability of sodium bicarbonate and carbonate ion pairs to 200°C – A potentiometric and spectrophotometric study'.

1290 In: *Geochimica et Cosmochimica Acta* 120, pp. 600–611. ISSN: 00167037.
1291 DOI: 10.1016/j.gca.2013.04.023.
1292 Tanger, J. C. and H. C. Helgeson (Jan. 1988). ‘Calculation of the thermo-
1293 dynamic and transport properties of aqueous species at high pressures
1294 and temperatures; revised equations of state for the standard partial molal
1295 properties of ions and electrolytes’. In: *American Journal of Science* 288.1,
1296 pp. 19–98. ISSN: 0002-9599. DOI: 10.2475/ajs.288.1.19.